J. Fluid Mech. (1996), *vol.* 322, *pp.* 243–273

Rapidly rotating turbulent Rayleigh–Bénard convection

By K. JULIEN[1,2], S. LEGG[1,2]†, J. McWILLIAMS[2] AND J. WERNE[2]

[1]Joint Institute for Laboratory Astrophysics, University of Colorado, Boulder, CO 80309, USA
[2]National Center for Atmospheric Research, Boulder, CO 80307, USA

(Received 12 September 1995 and in revised form 26 February 1996)

Turbulent Boussinesq convection under the influence of rapid rotation (i.e. with comparable characteristic rotation and convection timescales) is studied. The transition to turbulence proceeds through a relatively simple bifurcation sequence, starting with unstable convection rolls at moderate Rayleigh (Ra) and Taylor numbers (Ta) and culminating in a state dominated by coherent plume structures at high Ra and Ta. Like non-rotating turbulent convection, the rapidly rotating state exhibits a simple power-law dependence on Ra for all statistical properties of the flow. When the fluid layer is bounded by no-slip surfaces, the convective heat transport ($Nu - 1$, where Nu is the Nusselt number) exhibits scaling with $Ra^{2/7}$ similar to non-rotating laboratory experiments. When the boundaries are stress free, the heat transport obeys 'classical' scaling ($Ra^{1/3}$) for a limited range in Ra, then appears to undergo a transition to a different law at $Ra \approx 4 \times 10^7$. Important dynamical differences between rotating and non-rotating convection are observed: aside from the (expected) differences in the boundary layers due to Ekman pumping effects, angular momentum conservation forces all plume structures created at flow-convergent sites of the heated and cooled boundaries to spin-up cyclonically; the resulting plume/cyclones undergo strong vortex–vortex interactions which dramatically alter the mean state of the flow and result in a finite background temperature gradient as $Ra \to \infty$, holding Ra/Ta fixed.

1. Introduction

Turbulent convective motion under the influence of rotation is an important feature of many astrophysical and geophysical flows, from solar and giant planetary convection to oceanic deep convection. Each configuration possesses its own distinguishing features. For our Sun, for example, the convectively unstable layer (or convection zone) is deep, encompassing roughly the outer 25% of the sphere by radius, the inner 75% being convectively stable. Convective motions are driven by the continual heat generation in the solar interior, forcing the turbulent motions in the convecting layer in a statistically steady manner (Spiegel 1971, 1972). The great depth of the solar convection zone makes both fluid compressibility and the Sun's spherical geometry important ingredients in the fluid dynamics. Like the sun, the giant planets (Jupiter, Saturn, and Neptune) possess deeply convecting outer layers, also driven by (much weaker) internal radiative heat generation. Unlike the Sun, however, the giant planets rotate rapidly, resulting in the strong, alternating zonal jets

† Present address: University of California, Los Angeles, CA 90007, USA.

present in their atmospheres (Ingersoll 1990); the more weakly rotating Sun possesses just one zonal jet, i.e. the solar differential rotation.† Oceanic convection differs from these examples in its shallow depth and modest geographical extent; hence, incompressibility and a Cartesian-layer geometry can adequately approximate oceanic fluid dynamics. As opposed to the internal heat generation in the Sun and giant planets, the driving force for convection in the ocean results from temporally and spatially varying surface cooling instigated by seasonal changes in atmospheric conditions; therefore, ocean convection is inherently time-dependent, proceeding through the progressive erosion of the underlying stable fluid, and does not permit a statistically steady flow configuration (Stommel 1972; Schott, Visbeck & Fischer 1993). All of these flows are complicated in one way or another by details of the fluids involved: magnetic fields and ionization effects significantly influence solar convection, while salinity (in addition to temperature) is an active scalar field participating in ocean convection. Nevertheless, all the above phenomena share high Reynolds $Re = U\ell/\nu$ and low Rossby numbers $Ro = U/(\ell f)$, implying rotationally constrained turbulent convection. Here U and ℓ are characteristic flow velocities and lengthscales, ν is the fluid's kinematic viscosity and $f = 2\Omega$ is the Coriolis parameter where Ω is the external rotation rate. In contrast, convection in the Earth's atmosphere is associated with large Ro, and rotation can be ignored on the scale of the convecting elements (Deardorff 1970*a*, *b*; Klinger & Marshall 1995).

In order to investigate some of the general features of convection under the influence of strong rotation, we consider the paradigm of rotating Rayleigh–Bénard convection in which a uniformly rotating Boussinesq fluid (for which the effect of density variations is important only in fluid buoyancy) is bounded from above and below by horizontal planes held at fixed temperatures. We consider only the simplest case in which the direction of rotation is aligned with gravity. Such an arrangement avoids complicating features of the specific examples mentioned above, but maintains the essential ingredients shared by all of those flows: buoyancy and rotation. Also, for such a simple arrangement, the state of the flow is completely determined by specification of the boundary conditions and only four parameters: Ra, Ta, σ (the Prandtl number), and A (the domain aspect ratio). These parameters are defined as follows:

$$Ra = \frac{g\alpha \Delta L^3}{\nu\kappa}, \qquad Ta = \left(\frac{fL^2}{\nu}\right)^2, \qquad \sigma = \frac{\nu}{\kappa}, \qquad \text{and} \qquad A = \frac{L_x}{L},$$

where L and L_x are the depth and breadth of the layer, Δ is the imposed temperature difference between the bottom and top boundaries, and g is the local acceleration due to gravity; α and κ are the fluid's thermal expansion coefficient and thermal diffusivity, respectively. The non-dimensional numbers Ra and Ta measure the strength of the buoyancy force and external rotation applied to the fluid layer, while σ and A are properties of the fluid and the domain geometry.

In recent years, non-rotating Rayleigh–Bénard convection has received much attention as a model problem for transitions to turbulence. A thorough discussion of the linear stability problem is provided by Chandrasekhar (1961), while studies of transition to nonlinear chaotic flows abound (see Busse 1978 and references therein).

† Though mean flows are implicitly associated with rotating convection, the formation of zonal jet flows which match observations for the giant planets and the Sun remains a theoretical and numerical challenge (Busse 1983). In particular, the sustained energetic maintanence of jets and mean flows from turbulent convective sources is yet to be demonstrated.

At sufficiently high Ra (e.g. $Ra \gtrsim 4 \times 10^7$ in unit aspect ratio (Heslot, Castaing & Libchaber 1987)), convective turbulence prevails, but with a character quite different from early theoretical perceptions (Priestley 1959; Malkus 1963; Howard 1966); this so-called 'hard-turbulent' state of convection is defined by its heat-transport law ($Nu \sim Ra^{2/7}$), exponential temperature probability distributions at midlayer, and the thermal plumes responsible for the general character of the flow regime (Heslot *et al.* 1987). Though Rayleigh–Bénard convection has seen a resurgence in recent years, with intense experimental (Heslot *et al.* 1987; Castaing *et al.* 1989; Sano, Wu & Libchaber 1989; Zocchi, Moses & Libchaber 1990; Wu & Libchaber 1992; Tong & Shen 1992; Belmonte, Tilgner & Libchaber 1993; Tilgner, Belmonte & Libchaber 1993), theoretical (Castaing *et al.* 1989; She 1989; Shraiman & Siggia 1990; Yakhot 1992), and numerical work (DeLuca *et al.* 1990; Werne *et al.* 1991; Werne 1993; Christie & Domaradzki 1993, 1994; Cortese & Balachandar 1993; Kerr 1996), evidence for the existence of the hard-turbulent state can be found in the literature as early as 1969 (Rossby 1969).

Previous studies of rotating convection include the onset of convection at $Ra = Ra_c$, (Chandrasekhar 1953, 1961; Nagakawa & Frenzen 1955; Rossby 1969), and the convective dynamics at low supercriticality $S = (Ra - Ra_c)/Ra_c > 0$. As S increases, the transition to chaotic time-dependent behaviour proceeds from steady roll convection through the Küppers–Lortz instability (Küppers & Lortz 1969; Küppers 1970; Busse & Clever 1979), to convection dominated by complex spatial patterns and interacting vertical vortices (Li & Ecke 1993; Zhong, Ecke & Steinberg 1993; Rossby 1969; Boubnov & Golitsyn 1986, 1990). The chaotic cellular convection which results at moderate S has been studied numerically with a variety of vertical boundary conditions (Somerville & Lipps 1973; Raasch & Etling 1991; Cabot *et al.* 1990; Klinger & Marshall 1995); however no attempt has been made to systematically study the influence of these boundary conditions on the development of the flow. The experiments of Rossby (1969) and Zhong *et al.* (1993) indicate that at higher S the Nusselt number Nu is slightly increased compared to non-rotating values; they propose Ekman pumping as a possible cause. Recent experiments and simulations of unsteady turbulent convection forced by buoyancy loss at only one surface and influenced by strong rotation (Fernando, Chen & Boyer 1991; Jones & Marshall 1993; Maxworthy & Narimousa 1994; Helfrich 1994) have demonstrated the role of rotation in determining the characteristic length- and velocity scales for convection; however, similar questions have not yet been answered for the analogous problem of statistically steady plume-dominated rotating Rayleigh–Bénard convection. Here we complement previous studies by concentrating on higher-Re turbulent rotating Rayleigh–Bénard convection, providing a detailed examination of the influence of vertical boundary conditions on the dynamics of the statistically steady turbulent convecting state.

2. Numerical model

Before presenting our numerical solutions, we briefly discuss the numerical model with which the solutions are computed. The model problem incorporates the Boussinesq approximation (see Chandrasekhar 1961) for a rotating incompressible fluid:

$$\frac{\partial \boldsymbol{v}}{\partial t} + \left(\boldsymbol{\omega} + \sigma \left(\frac{Ta}{16}\right)^{1/2} \hat{\boldsymbol{z}}\right) \times \boldsymbol{v} = \sigma \nabla^2 \boldsymbol{v} - \nabla P + \sigma \frac{Ra}{16} T \hat{\boldsymbol{z}} \,, \tag{2.1}$$

$$\frac{\partial T}{\partial t} + \boldsymbol{v} \cdot \nabla T = \nabla^2 T \,, \tag{2.2}$$

$$\nabla \cdot \boldsymbol{v} = 0 \,. \tag{2.3}$$

The unit-vector $\hat{z}$ is directed vertically upward. The units of length, time and temperature used to express (2.1)–(2.3) in their non-dimensional form are $L/2$, $L^2/(4\kappa)$ and $\Delta/2$. The variables $\boldsymbol{v}$, T and P are the velocity, temperature and dynamic pressure head.† $\boldsymbol{\omega}$ is the curl of the velocity field (i.e. the vorticity). Solutions to (2.1)–(2.3) are computed in a rectilinear domain of dimensions $AL \times AL \times L$ using a pseudospectral Fourier–Chebyshev 'tau' method; see Appendix A.

The conditions imposed on the top and bottom boundaries are either no slip

$$\boldsymbol{v}(x, y, \pm 1) = 0 \,, \tag{2.4}$$

or stress free

$$\partial_z u(x, y, \pm 1) = 0 \,, \qquad \partial_z v(x, y, \pm 1) = 0 \,, \qquad w(x, y, \pm 1) = 0 \,, \tag{2.5}$$

with the temperature fixed

$$T(x, y, \pm 1) = \mp 1 \,. \tag{2.6}$$

All flows computed are periodic in the horizontal directions:

$$\boldsymbol{v}(x + L_x/L, y + L_y/L, z) = \boldsymbol{v}(x, y, z) \,, \tag{2.7}$$

$$T(x + L_x/L, y + L_y/L, z) = T(x, y, z) \,. \tag{2.8}$$

Here (x, y, z) and (u, v, w) are the spatial components of the coordinates and the velocity, respectively; z labels the vertical direction. The intent in using side boundaries which are periodic is to approximate an infinite horizontal extent (i.e. $A = \infty$); the degree to which this approximation succeeds is determined by the smallness (compared to AL) of the characteristic horizontal lengthscales appearing naturally in the solutions. Generally, the stronger the influence of rotation on convection, the smaller will be the horizontal lengthscales (Chandrasekhar 1961). All of our turbulent solutions exhibit $AL/\ell > 6$ where ℓ is the largest characteristic horizontal lengthscale; a few comparisons with different A show no significant effects.

A general study of rotating Rayleigh–Bénard convection requires the independent variation of the four parameters Ra, Ta, σ, and A as well as a determination of the influence of different boundary conditions (e.g. no slip or stress free) on the top and bottom surfaces. A reasonably complete survey of parameter space might include 10 data points for each of the four parameters listed above. This alone, i.e. without considering different boundary conditions, amounts to 10^4 separate simulations, clearly an unrealistic undertaking for a single numerical study. Therefore, to focus the present work, we have chosen to restrict our solutions to $\sigma = 1$ and $A = 2$ (unless otherwise noted) and to vary Ra and Ta such that the influence of rotation remains important and comparable for all values of the buoyancy forcing (Ra). We do this by equating a fraction of the rotation time $t_R = f^{-1}$ with the vertical advection time $t_W = h/W$, where h is the characteristic vertical lengthscale of the convective motion, and W is the vertical velocity scale. This results in the constraint

† The temperature and pressure in (2.1) and (2.2) are related to their more conventional definitions (T', P') by the following: $T = (T' - T_o)/(\Delta/2)$ and $P = (P'/\rho + v^2/2 + gz')L^2/(4\kappa^2)$, where T_o is the average of the temperatures at which the top and bottom boundaries of the fluid are held, ρ is the mean density of the fluid, and z' is the vertical distance measured from the middle of the domain.

$t_R/t_W = W/(fh) =$ constant, implying that a fluid parcel undergoes a fixed number of revolutions due to the external rotation Ω as it traverses the distance h. Holding this ratio of timescales constant as Ra is increased is equivalent to fixing the *convective* Rossby number:

$$Ro = \frac{W}{fh}.$$

Estimating W from the classic 'free-fall' relation (Prandtl 1932):

$$\tfrac{1}{2}W^2 = g\alpha \Delta_T h, \tag{2.9}$$

where Δ_T is the thermal contrast of a fluid element, we obtain $W \approx (g\alpha\Delta h)^{1/2}$ (presuming intensely buoyant fluid elements to possess characteristic temperatures $\Delta_T \approx \Delta/2$). With the choice of $h = L$ (the depth of the layer), we obtain an expression for Ro:

$$Ro = \left(\frac{Ra}{\sigma Ta}\right)^{1/2}. \tag{2.10}$$

This form of Ro was first used by Gilman (1977) and then later by Hathaway, Toomre & Gilman (1980), Cabot *et al.* (1990), Cabot & Pollack (1992), and Brummell, Toomre & Hurlbert (1996). Other definitions for Ro result from different choices of W and h. For example, penetrative convection in a semi-infinite domain (appropriate to the ocean surface or the base of the solar convection zone) has no externally imposed lengthscale; therefore one appearing naturally in the flow should be chosen, e.g. the depth of the penetrative zone or mixed layer. A reasonable choice for the velocity scale W for penetrative convection is the turbulent convective velocity scale $W_* = (B\,\ell_m)^{1/3}$ of Deardorff (1970*a*, *b*). Here B is the buoyancy flux and ℓ_m is the depth of the mixed layer. This results in Ro defined by $[Ra_f/(\sigma^2 Ta^{3/2})]^{1/3}$ (Maxworthy & Narimousa 1994), where the flux Rayleigh number is $Ra_f = B\ell_m^4/(\nu\kappa^2)$. For deep convection for which rotation may constrain the vertical transport, $W \sim (B/f)^{1/2}$ has been suggested as appropriate to define a 'natural' Rossby number $Ro_* = [Ra_f/(\sigma^2 Ta^{3/2})]^{1/2}$, differing from the previous definition in exponent only† (Raasch & Etling 1991; Fernando *et al.* 1991; Jones & Marshall 1993; Maxworthy & Narimousa 1994). Regardless of the particular definition of the convective Rossby number, smaller values indicate a greater influence of rotation on the dynamics, while larger values indicate the dominance of buoyancy over rotation. Note, all forms presented are independent of molecular properties ν and κ. For our study we have chosen an intermediate value, $Ro = 3/4$ (per (2.10)), for which both buoyancy and rotation are important.

The parameters used for the simulations reported here are presented in table 1. Almost all of the calculations are conducted with $A = 2$, though we expand A to be as large as $A \approx 5$ when computing weakly nonlinear solutions, and we reduce A to 1 for our highest-Ta calculations ($Ta = 3.2 \times 10^8$). The characteristic horizontal scale ℓ decreases with increasing Ta (Chandrasekhar 1961). At $Ta = 3.2 \times 10^8$, the mean 'cell-size' is $L/5$ and calculation with $A = 2$ simply becomes unnecessarily exorbitant. We have checked that a reduction of A from 2 to 1 does not alter the time-averaged solutions for the lower $Ta = 1.0 \times 10^8$, whose fluid structures are larger than those observed at $Ta = 3.2 \times 10^8$.

The choice of the number of spectral modes in each spatial direction (N_x, N_y, N_z)

† The analogous rotationally constrained velocity for the rotating Rayleigh–Bénard problem is $g\alpha\Delta/f$, resulting in $Ro_* = Ra/(\sigma Ta)$.

Ra	Ta	Ra_{crit}	k_0L	Spectral modes	Boundaries
3.09×10^4	5.50×10^4	1.17×10^4	6.5	$64 \times 64 \times 33$	no slip
7.03×10^4	1.25×10^5	1.91×10^4	7.5	$96 \times 96 \times 49$	no slip
2.81×10^5	5.00×10^5	4.55×10^4	9.6	$96 \times 96 \times 49$	no slip
5.91×10^5	1.05×10^6	7.34×10^4	10.9	$96 \times 96 \times 49$	no slip
2.53×10^6	4.50×10^6	1.91×10^5	14.2	$128 \times 128 \times 65$	no slip
8.44×10^6	1.50×10^7	4.53×10^5	17.6	$128 \times 128 \times 65$	no slip
2.81×10^7	5.00×10^7	9.56×10^5	21.8	$192 \times 192 \times 97$	no slip
1.13×10^8	2.00×10^8	2.44×10^6	27.9	$384 \times 384 \times 193$	no slip
5.63×10^4	1.00×10^5	2.13×10^4	8.6	$96 \times 96 \times 49$	stress free
1.97×10^5	3.50×10^5	4.70×10^4	10.7	$96 \times 96 \times 49$	stress free
5.63×10^5	1.00×10^6	9.22×10^4	12.9	$128 \times 128 \times 65$	stress free
1.97×10^6	3.50×10^6	2.08×10^5	15.9	$192 \times 192 \times 97$	stress free
5.63×10^6	1.00×10^7	4.15×10^5	19.0	$192 \times 192 \times 97$	stress free
1.97×10^7	3.50×10^7	9.47×10^5	23.5	$256 \times 256 \times 129$	stress free
5.63×10^7	1.00×10^8	1.90×10^6	28.0	$256 \times 256 \times 129$	stress free
1.78×10^8	3.16×10^8	4.07×10^6	34.0	$256 \times 256 \times 257$	stress free

TABLE 1. Parameters for the simulations. Ra_{crit} is the 'critical' Rayleigh number for the onset of convection. k_0L is the magnitude of the normalized horizontal wavevector for the most unstable linear mode at onset. 'Spectral modes' refers to the number of Fourier or Chebyshev polynomials used in each spatial direction ($x \times y \times z$). All simulations are conducted with a domain aspect ratio of $A = 2$ (i.e. $2 \times 2 \times 1$), except for the highest-Ta stress-free calculation, which has $A = 1$. At this highest value of $Ta = 1.8 \times 10^8$, k_0L is sufficiently high for $A = 2$ to be unnecessary.

is guided by the magnitude of the Kolmogorov lengthscale for the flow:

$$\ell_K = \left(\frac{\nu^3}{\epsilon}\right)^{1/4},$$

where $\epsilon = \nu \langle \partial_i \tilde{v}_j \partial_i \tilde{v}_j + \partial_i \tilde{v}_j \partial_j \tilde{v}_i \rangle$ is the time-averaged kinetic energy dissipation rate for the velocity fluctuations $\tilde{v}_i$. All of our calculations are performed with a ratio of the grid spacing δr to the Kolmogorov scale of $\delta r/\ell_K < 1.5$ in each spatial direction. We should point out that our choice of N_z, in addition to adequately resolving the Kolmogorov scale of the turbulence, also resolves the thin thermal boundary layers attached to the top and bottom boundaries of the domain with at least 12 collocation (grid) points. In this respect, the non-uniform distribution of Chebyshev collocation points (Canuto *et al.* 1988) is advantageous. Though convection between no-slip boundaries has previously been handled with algorithms similar to ours (see Canuto *et al.* 1988 and references therein), we are unaware of the use of Chebyshev methods for convection between stress-free boundaries. Typical spectral algorithms for stress-free boundaries employ Fourier methods which use uniformly spaced collocation points (e.g. Riley, Metcalfe & Orszag 1986). In the case of convection, however, uniform grids typically provide only very few grid points to resolve the thermal boundary layers (e.g. Cortese & Balachandar 1993 use sine-expansions for the temperature field and allow less than two grid spacings in the thermal boundary layer), resulting in erroneous computation of the heat flux through the layer. We are confident that the solutions we present here are the most accurate and highest-Ra direct numerical simulations of Rayleigh–Bénard convection conducted to date.

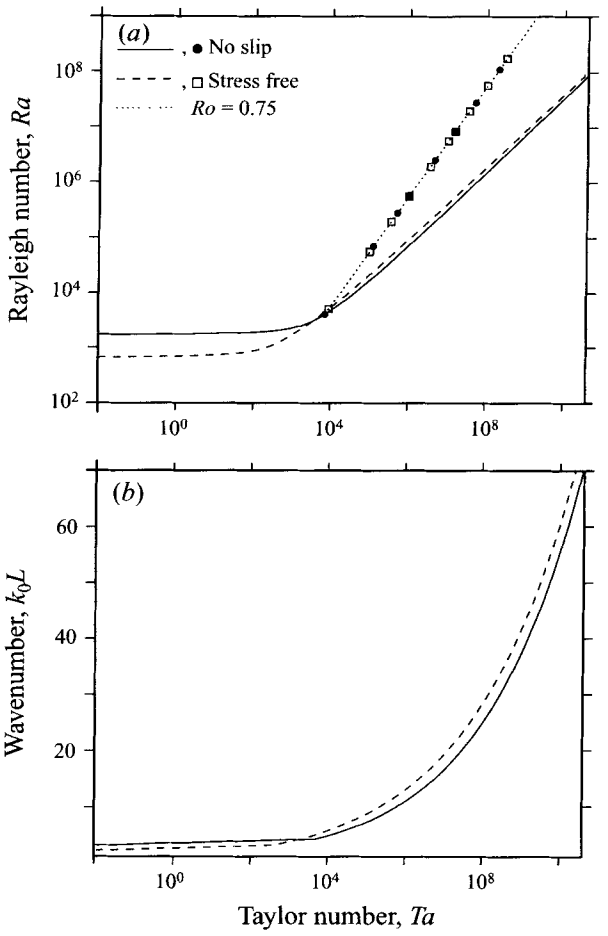

FIGURE 1. (*a*) Ra_c versus Ta for both no-slip and stress-free boundary conditions. (*b*) The most unstable linear wavevector k_0L as a function of Ta. The parameter space we explore numerically is also shown: $Ro = [Ra/(\sigma Ta)]^{1/2} = 0.75$, where $\sigma = 1$.

3. Numerical results

3.1. *Transition to turbulence*

As Ra is increased, the flow undergoes a succession of transitions before reaching a turbulent state. The first transition is from the static, conducting state ($\boldsymbol{v} = 0$, $Nu = 1$) to a convecting flow. Since the critical Rayleigh number Ra_c for this transition depends not only on the choice of vertical boundary conditions (stress free or no slip) but also upon Ta (see figure 1; see also Chandrasekhar 1961), the value of Ra_c that we observe is fixed by our choice of $Ro = 3/4$. Of course to reproduce the linear stability prediction of $Ra_c = 4050$ ($Ra_c = 5074$) for no-slip (stress-free) bounding planes extending infinitely in the horizontal directions, we must be careful to choose the aspect ratio A commensurate with the most unstable horizontal mode. Therefore, to partially validate our computer program, we have relaxed the constraint $A = 2$ for these low-Ra solutions and selected $A = 5\lambda_o/L$, where the wavelength of the most unstable linear mode is $\lambda_o = 1.39L$ ($\lambda_o = 1.12L$) for no-slip (stress-free) boundaries. In this way we observe a transition from the static state between $Ra_c = 4049$ and

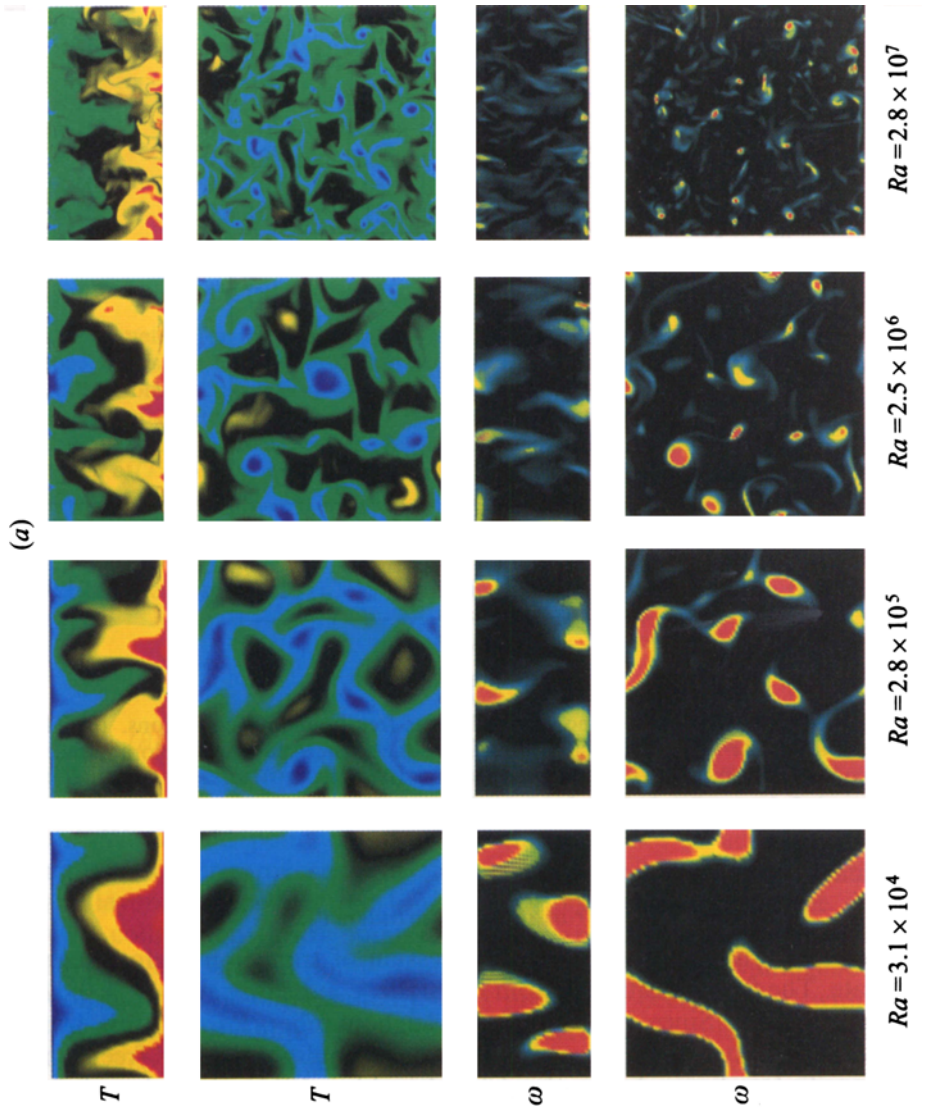

FIGURE 2. For caption see facing page.

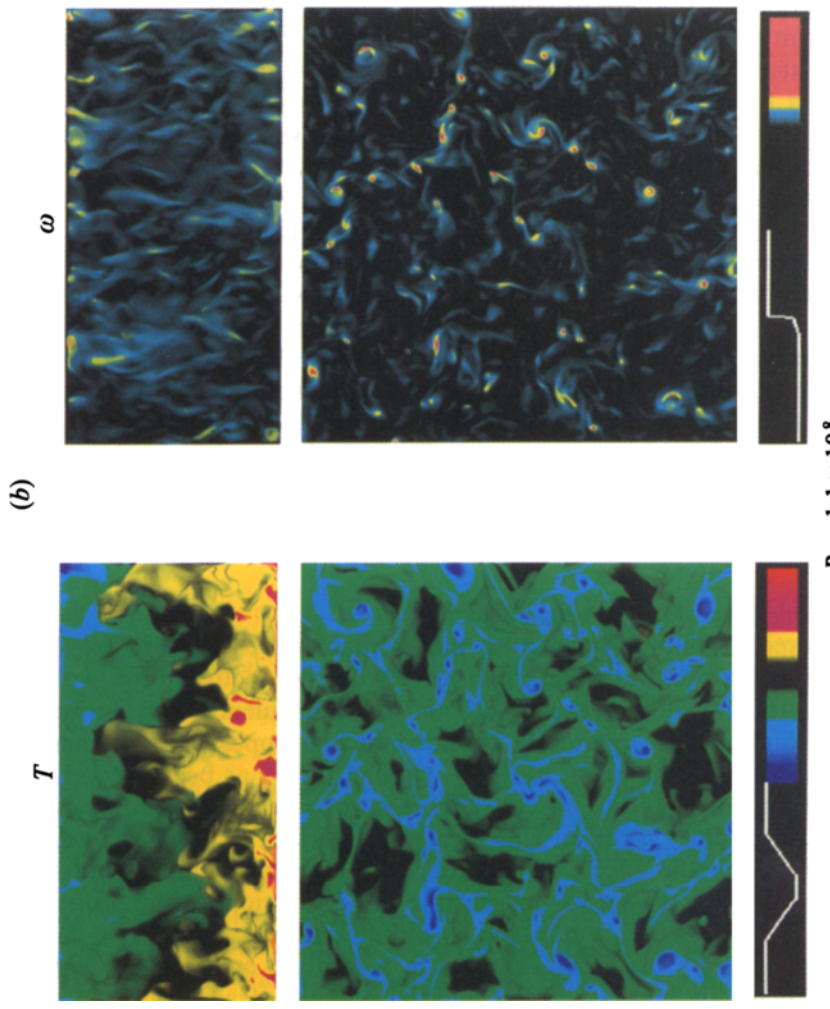

FIGURE 2. Flow-field development depicted by temperature T and vertical vorticity ω: $Ra = 3.1 \times 10^4$, unsteady rolls; $Ra = 2.8 \times 10^5$, interacting vortices; $Ra \geqslant 2.5 \times 10^6$, plume-dominated convection. All fields shown are for no-slip top and bottom boundary conditions with $Ro = [Ra/(\sigma Ta)]^{1/2} = 0.75$. The top two rows show T viewed from the side and from above on a plane just beneath the top boundary layer. Hot (cold) fluid is shown in red and yellow (blue and green). Neutral temperatures are black. The bottom two rows show ω for the same views as T. Intense cyclonic vorticity is shown in red. Weaker cyclonic vorticity is yellow. All anticyclonic vorticity is black. Note the reduction in the size and spacing of plumes as Ra is increased. Also note the strong localization (high skewness) of cyclonic vorticity in the plumes.

4051 (Ra_c = 5073 and 5075) for no-slip (stress-free) boundaries, consistent with the linear stability predictions.

The nature of the resulting convecting state is similar for the no-slip and stress-free boundaries. For $Ra > Ra_c$, we find that two-dimensional rolls are always Küppers–Lortz unstable, the loss of stability being to oblique rolls oriented at finite angles. These results are consistent with finite-amplitude predictions (Busse & Clever 1979; Clune & Knobloch 1993; Goldstein *et al.* 1994). Note that the stress-free solutions also possess an additional instability to *infinitesimal* angles (Swift 1984; Clune 1993), though this is difficult to observe numerically given that this instability possesses a smaller growth rate than that for finite angles.

As Ra is increased further, the aperiodic convection-roll patterns associated with the Küppers–Lortz instability (figure 2*a* for $Ra = 3.1 \times 10^4$; also Clever & Busse 1979; Li & Ecke 1993) gradually give way to a state dominated by the chaotic interaction between vertical vortices associated with convection cells (figure 2*a* for $Ra = 2.8 \times 10^5$; also Zhong *et al.* 1993; Boubnov & Golitsyn 1986). The general features of this space-filling pattern of chaotic cellular convection persist with increasing Ra until $Ra \approx 6 \times 10^5$ when coherent structures, i.e. thin thermal plumes, first appear spontaneously in the flow field (figure 2*a* for $Ra > 6 \times 10^5$). The plumes develop out of a buoyant instability of the thermal boundary layers and are most prevalent near the junctions of convection cells where cell boundaries merge with the thermal boundary layers attached to the heated and cooled (top and bottom) surfaces of the fluid layer (Adrian, Ferreira & Boberg 1986). Once $Ra > 2 \times 10^6$, the dynamics of the flow field are dominated by coherent plumes and the cellular convection itself becomes more difficult to discern, other than to simply note a mean distance between plumes; compare $Ra = 2.8 \times 10^5$ with 2.5×10^6, 2.8×10^7 and 1.1×10^8 in figure 2(*a*, *b*).

3.2. *Cyclonic plumes*

It is well known, especially for non-rotating fluids, that convection with strongly coherent thermal plume structures differs markedly from convective flows without plumes; for example, the transition between 'soft' and 'hard turbulence', two convective regimes existing at high Ra, is apparently heralded by the appearance of thermal plumes (Heslot *et al.* 1987; Castaing *et al.* 1989). Though there has been a good deal of work on the influence of rotation on convection, surprisingly little addresses the importance of thermal plumes to mean statistical properties of rotating convection and even fewer make clear the effects of rotation on the thermal plumes and their transport properties. For this reason we concentrate our discussion on the properties we observe for rotating convection dominated by thermal plumes.

The most striking property of thermal plumes in a rotating environment is their relative cyclonic vorticity, i.e. vorticity in the rotating reference frame with the same sign as the externally applied rotation Ω; see figure 3. This cyclonicity arises naturally as the boundary-layer fluid, which is initially stationary in the rotating frame (i.e. rotating at Ω with respect to an inertial frame), is drawn away from the boundary by buoyancy at plume formation sites. The vorticity in the plume intensifies as the horizontally convergent flow feeding it approximately conserves angular momentum, which is required during the formation of all plumes developing in a time short compared to their viscous diffusion time. This is not to say that anticyclonic plumes are forbidden; for example, in the limit $\Omega \to 0$, we expect plumes possessing both signs of vorticity. Nevertheless, when rotational effects are (even moderately) important, i.e. when Ω is greater than the root-mean-squared (RMS) vorticity which would occur naturally for non-rotating convection, anticyclonic plumes are unlikely. In addition,

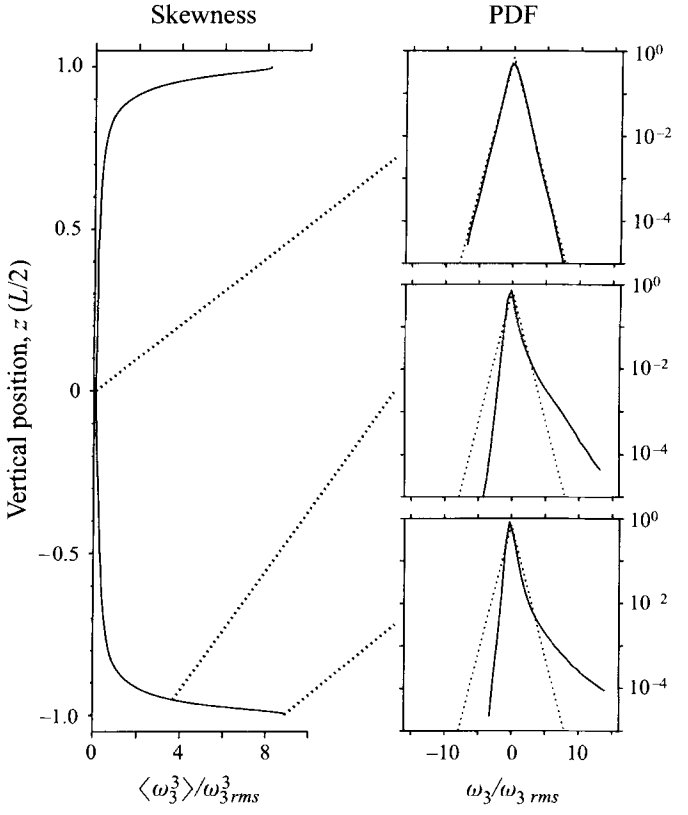

FIGURE 3. Skewness and PDFs of vertical vorticity ω_3 at different depths: $z = -0.999$ (within thermal boundary layer), $z = -0.952$ (just outside thermal boundary layer), $z = 0$ (mid-depth); $Ra = 1.125 \times 10^8$, and boundary conditions are no slip; results for stress-free boundaries are qualitatively similar. Normalized exponential PDFs are also included for comparison (dotted curve).

in the event that generation of strongly anticyclonic vorticity were to occur, vortices with $\omega < -\sigma(Ta/16)^{1/2}$ (or, with its usual dimensions, $\omega' < -f$) are inertially unstable (Ooyama 1966) and therefore would not remain coherent for long.

At this point it is important to note that even a requirement that all plumes be cyclonic does not exclude the occurrence of anticyclonic vorticity somewhere in the fluid layer; in fact, for periodic (or no-slip) horizontal boundary conditions the average vertical vorticity on horizontal planes must be zero. Hence, intense cyclonic vorticity is concentrated in thin thermal plumes while weak anticyclonic vorticity is spread throughout the remainder of the fluid layer, skewing the angular momentum distribution towards cyclonic, especially near the boundaries where plume formation is prevalent; see figure 3. Near midlayer, the vertical vorticity is nearly symmetric (i.e. skewness ≈ 0), indicating a dramatic reduction in the number of intense, isolated, cyclonic vortices as one moves away from the boundaries into the interior of the layer where turbulent motions mix the cyclonic vortices with ambient anticyclonic fluid.

3.3. *Ekman pumping*

In a rapidly rotating fluid layer, the cyclonic nature of plumes imposes important constraints on the dynamics of the flow near the boundaries, and as a result, many

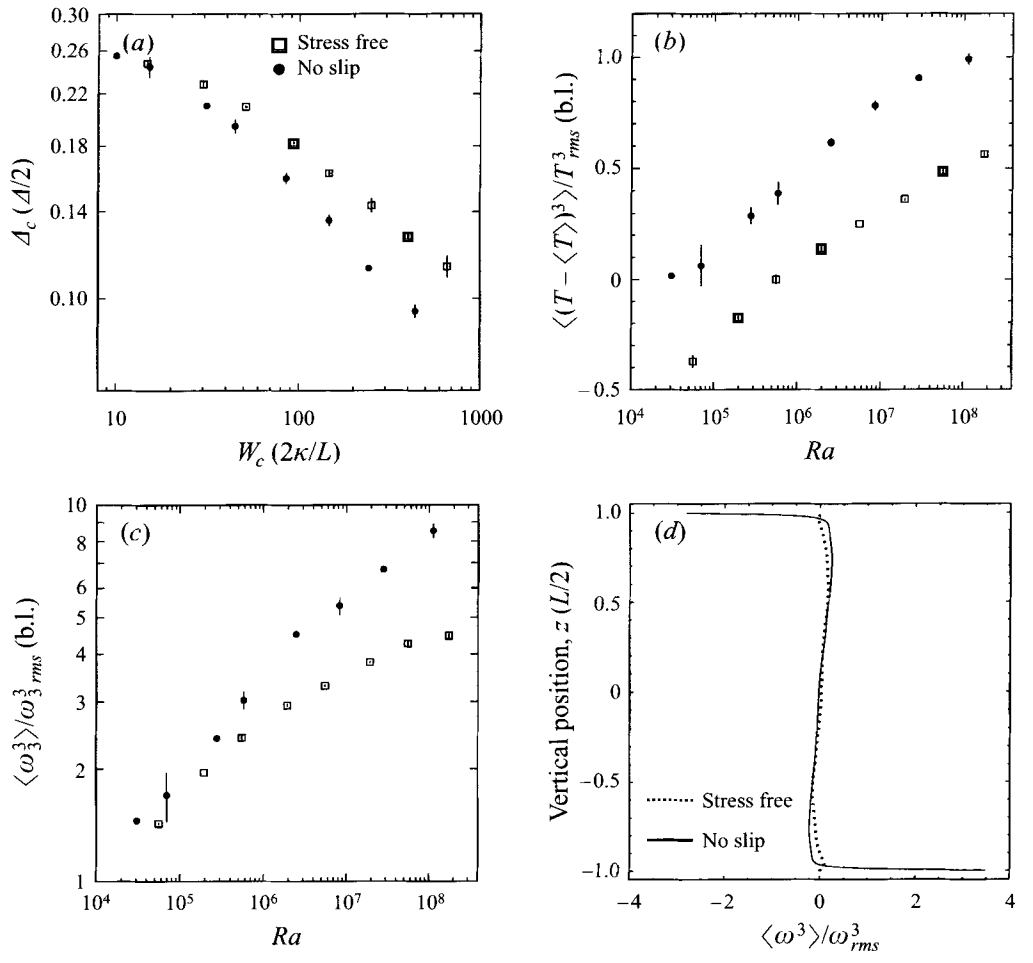

FIGURE 4. Intense Ekman pumping over no-slip boundaries; $\sigma = 1.0$, $[Ra/(\sigma Ta)]^{1/2} = 0.75$. (*a*) RMS temperature fluctuations at mid-depth Δ_c versus RMS vertical velocity fluctuations at mid-depth W_c. (*b*) Temperature skewness just outside the bottom thermal boundary layer where plumes develop. For high Ra, the skewness exhibits a local maximum at this location. Note that this particular plot is on a log-linear scale for which straight lines depict logarithmic dependence on Ra. (*c*) Maximum vertical vorticity skewness in the boundary layer versus Ra. (*d*) Profile of the vertical velocity skewness with height for no-slip ($Ra = 1.1 \times 10^8$) and stress-free ($Ra = 1.8 \times 10^8$) solutions.

statistical differences exist between the no-slip and stress-free solutions; see figure 4. The RMS temperature fluctuations at a given Reynolds number (figure 4*a*) are smaller for no-slip than for stress-free conditions, indicating that plumes are emitted with lower thermal contrast in the no-slip solutions. The temperature and vertical vorticity fields near the edge of the boundary layer (figures 4*b* and 4*c*) are much more strongly skewed in favour of the emitting plumes in the no-slip solutions, indicating that the presence of the no-slip boundary allows increased convergence of fluid in the boundary layer, and hence more strongly localized plume structures. In addition the vertical velocity field in the boundary layer is strongly skewed in the direction away from the boundary in the no-slip solutions, in contrast to the stress-free solutions which exhibit negligible velocity skewness (figure 4*d*). The difference indicates the presence of narrow jets associated with the emitting plumes for the no-slip case. These

differences are due to the existence of an intense shear-driven Ekman layer in the presence of the no-slip boundary. (While no-slip boundaries develop Ekman layers as a direct result of surface stress, stress-free boundaries only possess Ekman layers in the presence of horizontal thermal gradients; see Appendix B and Hide 1964.)

Classical linear Ekman-layer analysis (Ekman 1905; Gill 1982) shows that a cyclonic vortical flow (e.g. a tornado) in contact with a rotating no-slip boundary leads to ejection of fluid in a narrow jet in the centre of the vortex. In this linear hydrostatic theory, the vortex field far from the boundary is presumed to be in geostrophic balance with the radial pressure gradient, while close to the no-slip boundary, the azimuthal flow is reduced by friction. A radially spiralling inflow results from the excess pressure gradient; hence by continuity (2.3) there must be a flow away from the boundary at the centre of the vortex. This transport of mass away from the boundary is known as Ekman pumping. The analytic solution for the classic linear Ekman layer has the form $X = q^{-1}\partial_z X_0(1 - e^{-qz})$, where X is the horizontal velocity in complex notation $X = u + iv$ and q^{-1} is the complex Ekman layer thickness $q = 1/2(-Ta)^{1/4}$. $\partial_z X_0$ is the surface stress.

Our solutions are considerably more complicated than this idealized vortex: the flows are strongly nonlinear, non-hydrostatic, occur in connection with significant buoyancy, and are far from stationary and axisymmetric. In order to obtain a qualitative understanding of the effect of buoyancy on the Ekman velocities, we have performed a linear hydrostatic analysis of an Ekman layer in association with a thermal boundary layer; see Appendix B. We find that the classical Ekman solutions combine with a thermal-wind-type solution. Interestingly, the leading-order (i.e. linear) contribution of a raised bump on the thermal boundary layer (intended to model a developing plume) is to *inhibit* the growth of the bump through Ekman *suction* (as opposed to pumping) at the centre of the bump. Figure 5 shows a comparison of the temperature, horizontal divergence, and vertical vorticity predicted by the analysis with our numerical solutions. Lighter shades depict more intense temperature (e.g. hot just above the bottom boundary), horizontal convergence, and cyclonic flow. The horizontal divergence shows convergent flow (related to Ekman pumping) in a ring at the 'edge' of a plume, while divergent flow is apparent in the core region of a plume. Also, the linear analysis predicts that the convergent rings should be strongly cyclonic, which is indeed the case. In contrast, the core region of a plume is intensely anticyclonic for the linear analysis, while the same region is only less cyclonic in the numerical solutions. The discrepancy lies in the assumed bump-like shape of a plume in the linear analysis, while plumes are more ring-like in the simulations. The Gaussian-bump geometry assumed in the illustrative example concentrates too great a pressure in the plume core; see Appendix B. Also, it should be noted that the lack of the classic shear contribution to the Ekman layer for the stress-free solutions makes these boundaries more suitable for comparison with the linear thermal-Ekman solutions than no-slip boundaries. Intense plumes will of course be strongly nonlinear, reducing the applicability of the analysis discussed here; nevertheless, as figure 5 demonstrates, within the boundary layers some of the qualitative features of the linear analysis are apparent.

We can obtain a qualitative understanding of nonlinear effects by considering vortices in contact with a no-slip boundary. For example Carrier (1971) and McWilliams (1971) examine the nonlinear Ekman-layer problem for several radial profiles of vorticity, assuming in all cases hydrostatic balance, axisymmetric flow, and stationarity. All show that the nonlinearity of the flow causes the velocity spiral $[(u(z), v(z)]$ to curve inward more tightly as the surface stresses are increased relative

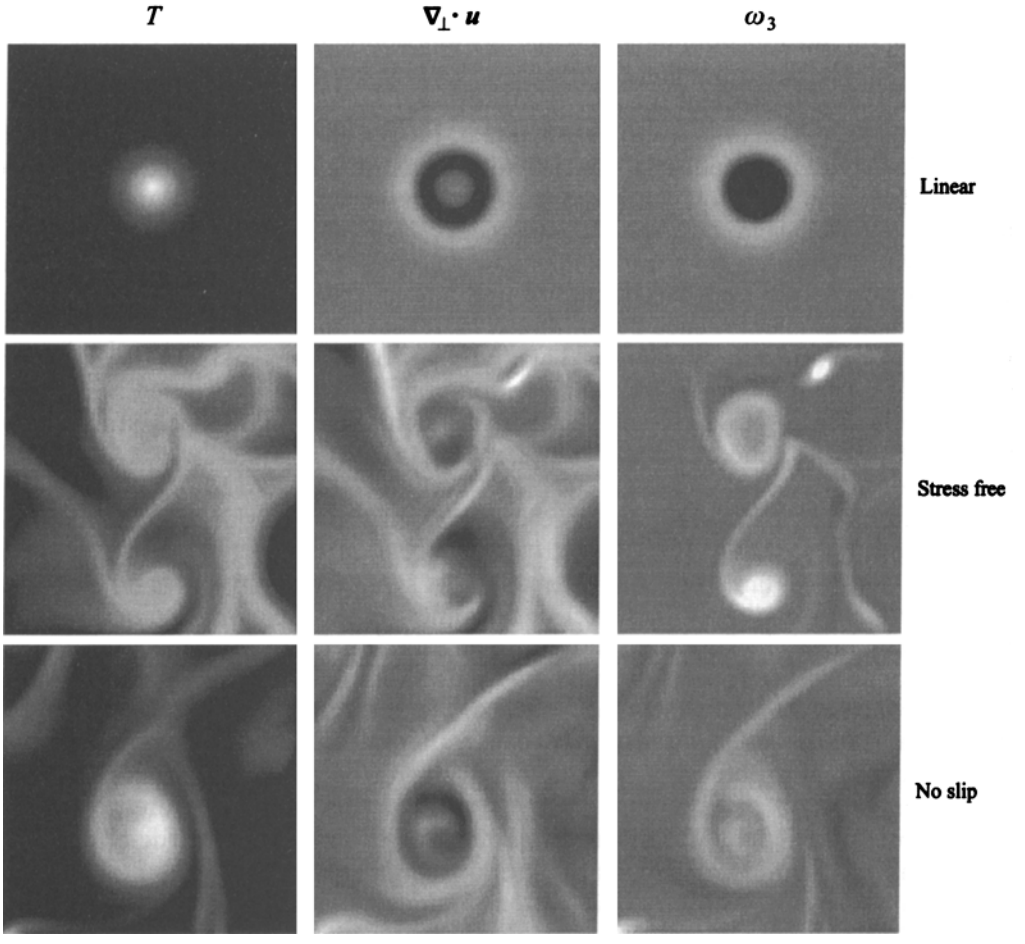

FIGURE 5. Temperature, horizontal divergence, and vertical vorticity on a horizontal plane through developing plumes. The top row depicts fields for the thermal Ekman layer resulting from a Gaussian-shaped 'plume' on the thermal boundary layer; see Appendix B. The middle (bottom) row displays fields for numerical simulations with stress-free (no-slip) boundaries within (slightly above) the mean hot thermal boundary layer. The shading is lighter for more intense temperatures (e.g. hot just above the bottom boundary), horizontal convergence, and cyclonic flow.

to the far-field flow. Furthermore, the vertical flow at the centre of the vortex tends to be concentrated in a narrower, more intense jet. Several non-hydrostatic simulations of an axisymmetric vortex attached to a no-slip boundary have been conducted in the study of tornado dynamics (Wilson & Rotunno 1986; Howells, Rotunno & Smith 1988). While these studies do not include external rotation, they indicate that a suction effect due to a pressure deficit in the vortex core is an important contribution in the fully non-hydrostatic case. Furthermore, the large radial inflow forces the vortex itself to become more strongly localized than would be possible in the absence of the frictional boundary layer; see figure 4(*c*).

Figure 6 shows several examples of 'Ekman spirals' ($v(z)$ versus $u(z)$) obtained for individual plumes in our numerical solutions. The solutions X are normalized by $q/\partial_z X_0$ so that comparison with the classic Ekman solution, as well as with solutions at different Ra, may be facilitated. While the linear theory appears to predict the shape

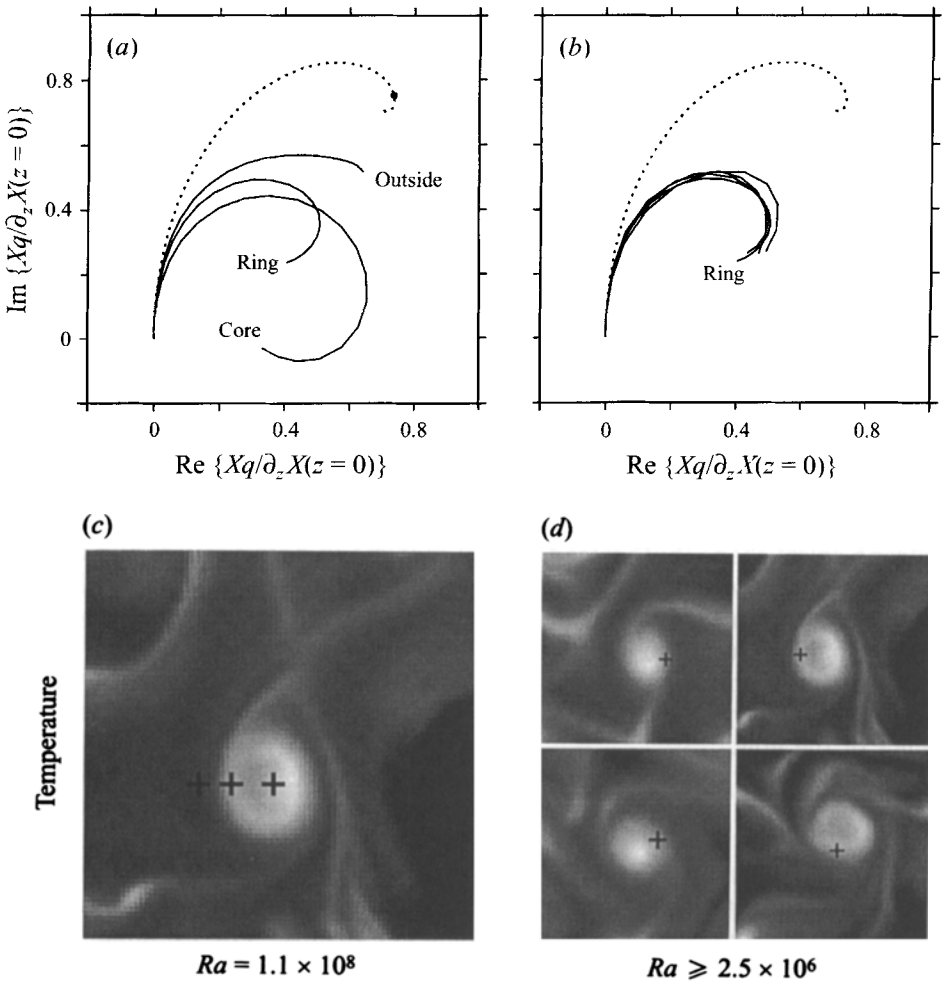

FIGURE 6. (a,b) Velocity hodographs $(v(x_i, y_i, z)$ versus $u(x_i, y_i, z)$ at a single horizontal location $(x_i, y_i))$ associated with plumes over no-slip boundaries. Hodographs are normalized by $q/\partial_z X_0$ and rotated 45° so they may be easily compared with the classic linear Ekman solution (dotted curve). X is the horizontal velocity in complex notation $X = u + iv$. q is the inverse of the complex Ekman layer thickness $q = \frac{1}{2}(-Ta)^{1/4}$. (a) Hodographs within the 'core' of a plume, in the 'ring' region at the edge of a plume, and just 'outside' a plume for $Ra = 1.1 \times 10^8$. The solid dot on the classic solution marks the height to which the simulations are plotted, roughly twice the thermal-boundary-layer thickness. Note that the numerical solutions spiral in more tightly than the linear solution, indicating the importance of nonlinear effects. (b) Hodographs in the ring region of plumes for high Ra ($Ra = 2.5 \times 10^6$, 8.4×10^6, 2.8×10^7 and 1.1×10^8). Note that all these solutions coincide, indicating a saturation of the nonlinear contribution within plume rings to a unique spiral structure. (c) Temperature on a plane just above the hot thermal boundary layer for $Ra = 1.1 \times 10^8$. Hotter fluid is depicted with lighter shades. Crosses indicate the locations of the hodographs in (a). (d) Temperature just above the hot boundary layer for the four values of Ra depicted in (b). Crosses mark the locations of hodographs plotted in (b). Ra increases from left to right with the highest Ra shown in the upper right corner and the lowest in the lower left.

of the profiles well, the numerical solutions spiral in more tightly and have lower interior velocities than the predicted geostrophic velocities, in qualitative agreement with the nonlinear and non-hydrostatic work quoted above. Figure 6(*a*) shows profiles at three distinct locations associated with a plume near a no-slip boundary for $Ra = 1.1 \times 10^8$: one in the core region, one in the ring region at the edge of the plume, and one just outside the plume; each region is depicted in figure 6(*c*) on a plane positioned just above the mean thermal boundary layer. While the core and outside regions exhibit substantial variability from plume to plume (due to different plume 'ages' and different instantaneous flow conditions external to the plume), the ring region appears better defined with similar Ekman spirals for different plumes. In fact, for sufficiently high Ra ($Ra \geqslant 2.5 \times 10^6$), the tightness of the Ekman spiral (i.e. the nonlinearity) in the ring region appears to saturate, producing spirals of nearly identical shape for plumes at different Ra; see figures 6(*b*) and 6(*d*). Solutions with $Ra < 2.5 \times 10^6$ exhibit weaker Ekman spirals, tending towards the classic linear solution as Ra (and hence, the nonlinearity) is decreased.

In summary, the observed (u, v) spirals give conclusive evidence for Ekman pumping in the no-slip rotating boundary layer. By contrast, the stress-free (u, v) fields show no such strong spiral shape, but instead exhibit maxima in both vortical and convergent flow at the boundary. The presence of a no-slip boundary, by allowing the angular momentum constraints to be partially overcome, allows greater convergence of fluid, and hence enables plumes to be more localized. In addition the narrow jet associated with Ekman pumping facilitates the emission of the plumes. The nature of the momentum boundary conditions is therefore crucial in determining the detailed dynamics of the flow.

3.4. *Scaling in the turbulent regime*

Despite these important differences arising directly from the nature of the top and bottom boundaries, the flow in the interior of the domain possesses some general features which are independent of the boundary details. For example, the classic description of a 'freely falling' fluid parcel is appropriate for our solutions. A freely falling fluid element is one which gains kinetic energy at the expense of buoyancy work, which is appropriate if the buoyancy time for the parcel is much less than either its thermal or viscous diffusion timescales. Figure 7 depicts the scaling of W_c and Δ_c (non-dimensional RMS vertical velocity and temperature fluctuations at midlayer) with Ra for simulations with both no-slip and stress-free boundaries. The scaling behaviour for these variables turns out to be

$$\Delta_c = C_1 Ra^{-\beta}: \qquad C_1 = \begin{cases} 1.25 \pm 0.17 \\ 1.16 \pm 0.06 \end{cases}, \quad \beta = \begin{cases} 0.140 \pm 0.008 & \text{no slip} \\ 0.107 \pm 0.004 & \text{stress free} \end{cases}, \tag{3.1}$$

$$W_c = C_2 Ra^{\gamma}: \qquad C_2 = \begin{cases} 0.15 \pm 0.01 \\ 0.17 \pm 0.01 \end{cases}, \quad \gamma = \begin{cases} 0.431 \pm 0.005 & \text{no slip} \\ 0.435 \pm 0.004 & \text{stress free} \end{cases}. \tag{3.2}$$

For the free-fall description to be correct, the exponents β and γ must obey (substituting Δ_c and W_c above for $2\Delta_T/\Delta$ and $WL/(2\kappa)$ in (2.9))

$$2\gamma = 1 - \beta\,, \tag{3.3}$$

which appears to be the case for both sets of boundary conditions. The stress-

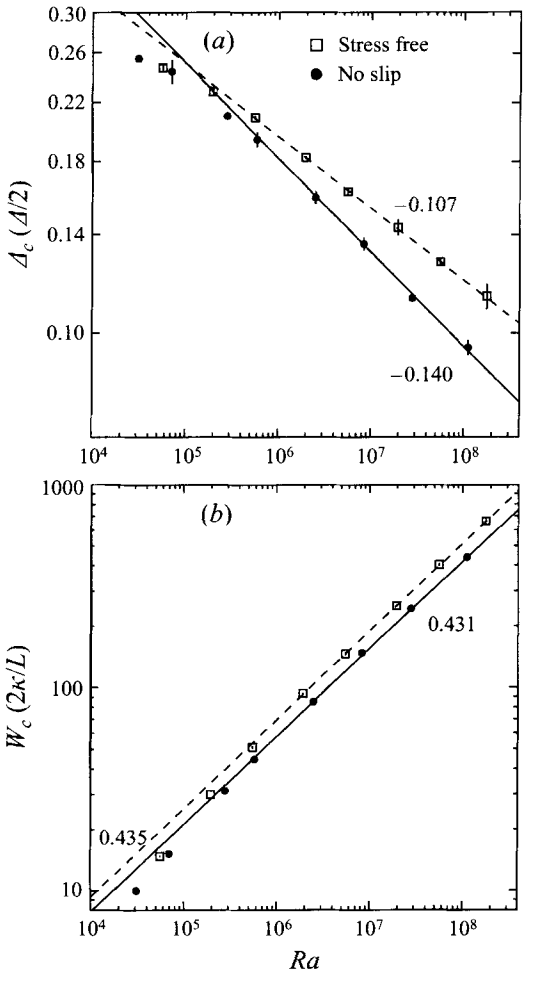

FIGURE 7. (*a*) W_c (RMS vertical velocity fluctuations at mid-depth) and (*b*) Δ_c (RMS temperature fluctuations at mid-depth) are shown for both no-slip and stress-free boundary conditions as a function of Ra. $\sigma = 1, [Ra/(\sigma Ta)]^{1/2} = 0.75$.

free solutions satisfy (3.3) only to within two standard deviations, while the no-slip solutions obey (3.3) within one standard deviation. Alternatively, this may indicate a slight deviation from free fall for the stress-free solutions; however, the effect is small. The occurrence of free-fall behaviour indicates that Ra is sufficiently high such that the dynamics of plumes in the interior are no longer controlled by details associated with the boundaries. This interpretation is further supported by probability density functions (PDFs) for various fields (velocity, vorticity, temperature): whereas the PDFs near the boundaries differ markedly for the two boundary conditions, near midlayer the PDFs are much more similar (figure 8).

We emphasize here that the scaling presented in (3.1)–(3.2) is measured with respect to Ra, not the supercriticality S. The distinction is unnecessary for non-rotating flows for which Ra_c = constant; however, since Ta differs for each of our runs, Ra_c also differs. The fact that the Δ_c- and W_c-scaling with Ra obeys (3.3), and furthermore that the exponents for the case with no-slip boundaries is consistent with $\beta = 1/7 \approx 0.1429$ and $\gamma = 3/7 \approx 0.4286$ (values associated with non-rotating

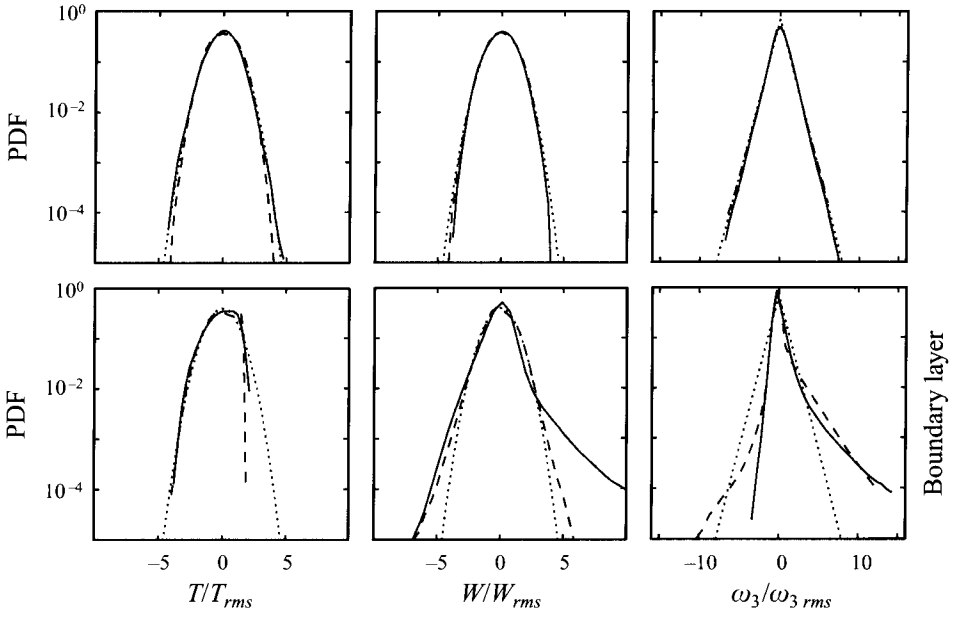

FIGURE 8. PDFs for temperature T, vertical velocity W, and vertical vorticity ω_3 are shown for no-slip boundaries at $Ra = 1.1 \times 10^8$ (solid curve) and stress-free boundaries at $Ra = 1.8 \times 10^8$ (dashed curve). Dotted Gaussian or exponential PDFs are also shown for comparison. The nature of the boundary conditions (no slip or stress free) greatly influences the shape of the PDFs within the boundary layer; however, at mid-layer, turbulent motions produce PDFs which are much more similar. Note that both W and ω_3 are strongly skewed towards ejected and cyclonic plumes in the boundary layer for the no-slip solutions, while T favours fluctuations from the bulk. T is skewed towards bulk temperature fluctuations because deep in the boundary layer the magnitude of potential hot fluctuations ($\approx \Delta/4$ at boundary-layer mid-height) is less than potential cold fluctuations from the bulk ($\approx 3\Delta/4$ at boundary-layer mid-height). Boundary-layer PDFs are shown at a depth equal to $0.5Nu^{-1}$. The temperature has been shifted by its horizontal average before constructing the boundary-layer PDF.

turbulent convection between no-slip boundaries, i.e. 'hard turbulence', Castaing *et al.* 1989), implies a relative unimportance of rotation for the vertical motions of the largest plumes near midplane. As we have already seen, rotation certainly does provide important and new dynamics to Rayleigh-Bénard convection; however, at midlayer these effects are most profound in the plane perpendicular to $\boldsymbol{\Omega}$ (which is parallel to $\boldsymbol{g}$ for our solutions) and are not competitive with buoyancy in determining vertical motions at midlevel for $Ro = 3/4$. This does not imply that Δ_c and W_c are independent of Ro; indeed, the coefficient C_1 for the no-slip solutions differs from that obtained in non-rotating laboratory flows (e.g. Wu & Libchaber 1992 obtain $C_1 = 1.9$ for a cylindrical cell with a diameter-to-height ratio of 6.7). The central turbulence dynamics certainly inherits a Ro-dependence from the near-boundary motions, which are strongly influenced by rotation. We examine the Ro-dependence of the dynamical quantities Δ_c and W_c in greater detail elsewhere (Julien *et al.* 1996*b*).

Because the scaling exponents, β and γ, are identical to the values for non-rotating high-Ra laboratory convection, the non-dimensional heat transport $Nu \approx \Delta_c W_c$ for our rotating solutions obeys the same relation observed for non-rotating fluid layers, namely $Nu \sim Ra^{2/7}$. Figure 9 demonstrates this law for our solutions between no-slip boundaries. A fit to Nu versus Ra for $Ra \geqslant 2.53 \times 10^6$ yields $Nu - 1 =$

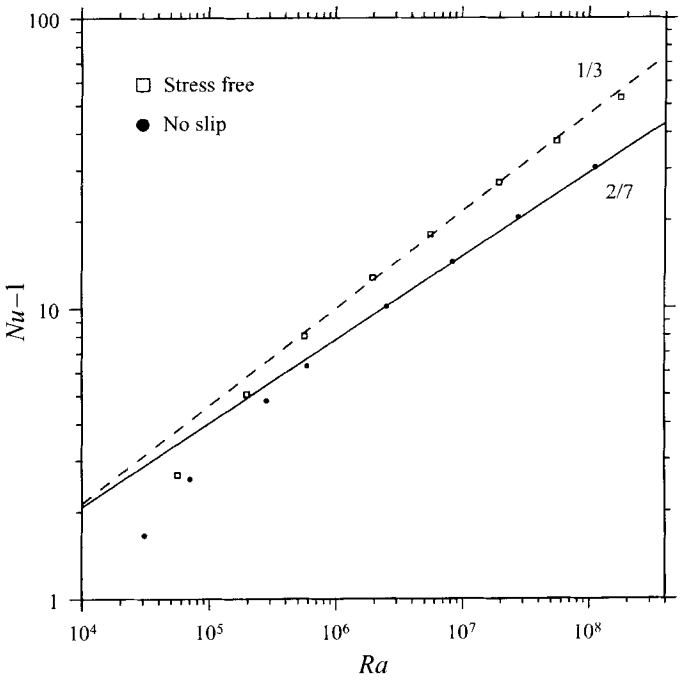

FIGURE 9. Convective heat transport ($Nu-1$) versus Ra for both no-slip and stress-free boundaries; $\sigma = 1.0, [Ra/(\sigma Ta)]^{1/2} = 0.75$. The uncertainty in Nu results from the finite numerical integration times used and is less than or equal to the size of the plotting symbols.

$(0.144 \pm 0.006)Ra^{0.288\pm0.003}$.† Zhong *et al.* (1993) and Veronis (1968) find that rotation slightly enhances the total heat transfer in Rayleigh–Bénard convection. Also, Wu & Libchaber (1992) report a general enhancement of the heat flux in non-rotating convection when the aspect ratio A of the fluid container is decreased; this trend is superposed with a local maximum in the heat transport near $A \approx 1$ (Wu & Libchaber 1992). Both effects (increased heat transport with increased rotation or decreased aspect ratio) may be related, given the decrease in the natural horizontal scale of convection cells as Ta is increased (see figures 1 and 2). It is difficult for us to make a direct comparison with the experiments (Zhong *et al.* 1993; Wu & Libchaber 1992) both because of the additional drag imposed by their physical no-slip side boundaries and because of the σ-dependence of the heat transfer; while we have used $\sigma = 1$ here, experiments of Zhong *et al.* employ water ($\sigma \approx 7$) and those of Wu & Libchaber use helium gas ($\sigma \approx 0.7$). Shriaman & Siggia (1990) suggest $Nu \propto \sigma^{-1/7}$, but this prediction is most appropriate when σ is asymptotically large, while here we discuss

† There is some inconsistency in the literature with regard to power-law fits of Nu to Ra^{β}. Whereas the initial experiments that reported hard-turbulent behaviour included fits of the convective flux or $Nu-1$ (Heslot *et al.* 1987; Wu *et al.* 1988), later work by the same group employed fits of the total flux, i.e. Nu without the -1 (e.g. Wu & Libchaber 1992). While the distinction can prove merely academic for large values of Nu – like those attainable in helium gas (Heslot *et al.* 1987) – for $Nu = O(10)$, such as those presented here, the fit parameters are affected by the exclusion of the -1. A more informative fit would be $Nu = N_1 + C(Ra^{\beta} - R_1^{\beta})$, or equivalently, $Nu = B + CRa^{\beta}$, with B varied so as to minimize the χ^2 of the fit. Of course, with the very few data points we can afford with numerical simulations, three-parameter fits are suspect. Nevertheless, in order to offer a bases of comparison for future work, a fit of this form to our numerical 'data' produces $Nu = -0.071 + (0.205 \pm 0.008)Ra^{0.271\pm0.003}$.

$\sigma \approx 1$. The stress-free solutions are also included in figure 9. They do not exhibit 2/7-scaling; rather they obey the 'classical' relation $Nu \propto Ra^{1/3}$ of Priestley (1959), Malkus (1963), and Howard (1966) in the range $10^6 < Ra < 4 \times 10^7$, then appear to undergo a transition to a less-efficient heat-transfer rate at higher Ra. Of course with such a limited range of possible scaling with Ra ($10^6 - 4 \times 10^7$), it is difficult to distinguish two power laws from a different functional form; however, it is clear that the initial behaviour of Nu for $Ra > 10^6$ differs between the no-slip and stress-free cases.

It is remarkable that the heat transport between no-slip boundaries for these strongly rotating solutions exhibits the same scaling as do experiments on non-rotating convection, especially given the additional influence of Ekman pumping for the rotating solutions. The early and excellent work of Rossby (1969) indicates the possibility of similar scaling behaviour for water ($\sigma \approx 7$) for which Nu was found to be only very weakly dependent on Ta when $Ra \gg Ra_c$. Why is the Nu–Ra scaling not modified by rotation for these turbulent solutions? The answer may lie in the fact that the stress-free solutions at least initially exhibit 1/3-scaling for the range in Ra where the no-slip solutions obey the 2/7-law (Julien *et al.* 1996*a*). Indeed, one theory for the heat-transport scaling in hard turbulence stresses the importance of strongly sheared thermal layers to establishing 2/7-scaling (Shraiman & Siggia 1990). This theory has detailed support from numerical simulations of non-rotating two-dimensional convection (Werne 1993) in which the sheared regions between plume sites are explicitly demonstrated to dominate the heat transport. Therefore, the heat transport would not be dominated by the enhanced ejection of plumes due to Ekman pumping, but rather by the sheared boundary-layer regions between plumes (resulting from cell-scale horizontal thermal winds, or alternatively, horizontal mixing motions due to vortical interactions between neighbouring plume/cyclones; see below). The lack of 2/7-scaling for the stress-free solutions in the range $10^6 < Ra < 4 \times 10^7$ supports this interpretation since stress-free boundaries do not support shears. However, the behaviour of Nu for $Ra > 4 \times 10^7$ is intriguing. Does rapidly rotating turbulent convection between stress-free boundaries obey $Nu \propto Ra^{2/7}$ for sufficiently high Ra? Unfortunately we cannot assess this for the solutions we compute because our highest Ra is only $Ra = 1.8 \times 10^8$, i.e. not sufficiently large to allow a substantial range of exploration above $Ra = 4 \times 10^7$. It is interesting to note, however, that the apparent Nu-transition at $Ra = 4 \times 10^7$ occurs when the mean thermal-boundary-layer thickness $\lambda = Nu^{-1}$ (expressed here in its non-dimensional form) equals the Ekman-layer thickness $\delta_E = 2Ta^{-1/4}$. (Convection over stress-free boundaries can possess Ekman layers if λ is not horizontally uniform; see Appendix B and Hide 1964.) Perhaps an argument similar to that of Shraiman & Siggia (1990) can predict the Nu–Ra relationship for turbulent rotating convection over stress-free boundaries. In addition, making use of the scaling behaviour of δ_E and λ, we expect a similar cross-over for the no-slip ($Ro = 0.75$) solutions at $Ra \approx 10^{16}$. We should note that the expression we employ for δ_E is an estimate and is not a lengthscale we observe directly in our solutions; therefore, we have not witnessed the cross-over of λ and δ_E for the stress-free solutions, but only hypothesize its existence.

3.5. *Lateral mixing and mean temperature gradients*

An example of the important role rotation can play in convection is demonstrated by figure 10, which depicts the mean temperature profile for increasing values of Ra. A striking difference between figure 10 and the analogous profiles for non-rotating convection is the finite value of the mean temperature gradient $|\partial_z T|$ in the interior of

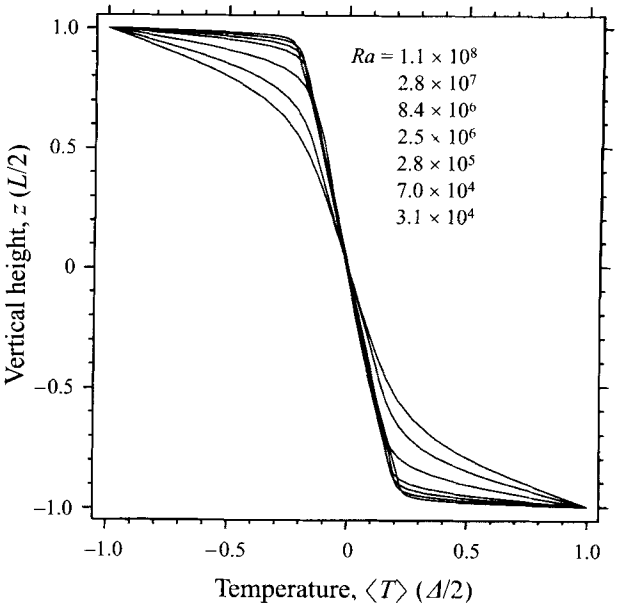

FIGURE 10. Profiles of mean temperature with height z; $\sigma = 1.0$; $[Ra/(\sigma Ta)]^{1/2} = 0.75$. All solutions shown possess no-slip boundaries. Higher-Ra solutions are distinguishable by their thinner boundary layers (with thickness $\lambda = Nu^{-1}$) at $z = \pm 1$. A mean negative thermal gradient persists in the interior at the highest Ra when $Ro = [Ra/(\sigma Ta)]^{1/2}$ is held fixed.

the layer which persists at large Ra; non-rotating convection does not support a mean negative temperature gradient (Tilgner *et al.* 1993; Belmonte *et al.* 1993). Figure 11 shows the magnitude of the gradient at mid-layer as a function of Ra. The negative gradient in the interior appears to asymptote to a finite value with increasing Ra for both no-slip and stress-free solutions (within the uncertainty resulting from the finite integration time for which we compute our solutions). Though the stress-free solutions may exhibit a slight trend in the gradient with Ra for high Ra, the uncertainty is larger than the gradient itself, and $|\partial_z T|$ independent of Ra at high Ra is consistent with the stress-free solutions. Hence in the high-Ra turbulent-plume regime, the value of the negative temperature gradient in the interior appears to depend only on the boundary conditions, Ro, and σ† (Julien *et al.* 1996*b*). These results are consistent with those of Fernando *et al.* (1991) who suggest the negative temperature gradient in rotating water-tank experiments is dependent on $f^2/(g\alpha)$ (or $(Q/\kappa)Ta\ \sigma/Ra_f$). Their experiments involve the time-evolution of a rotating fluid layer subjected to bottom heating Q switched on at $t = 0$. In contrast, Boubnov & Golitsyn (1990), conducting laboratory experiments of fixed-heat-flux rotating Rayleigh–Bénard convection, and Klinger & Marshall (1995), performing numerical simulations of rotating flux-driven ocean convection, both propose that the magnitude of the temperature gradient decreases substantially as Ra is increased, even when Ro is held constant.

The existence of a mean gradient for rotating turbulent convection is fairly easily understood, though the explanation involves two distinct steps. The first step is found in the discussion presented in detail above and requires only that plumes

† Preliminary rotating convection experiments in silicone oil ($\sigma = 8.4$) with $Ro = 0.75$ by Ohlsen, Hart & Kittelman (1995) demonstrate a σ-dependence of the mean thermal gradient when compared to our numerical solutions.

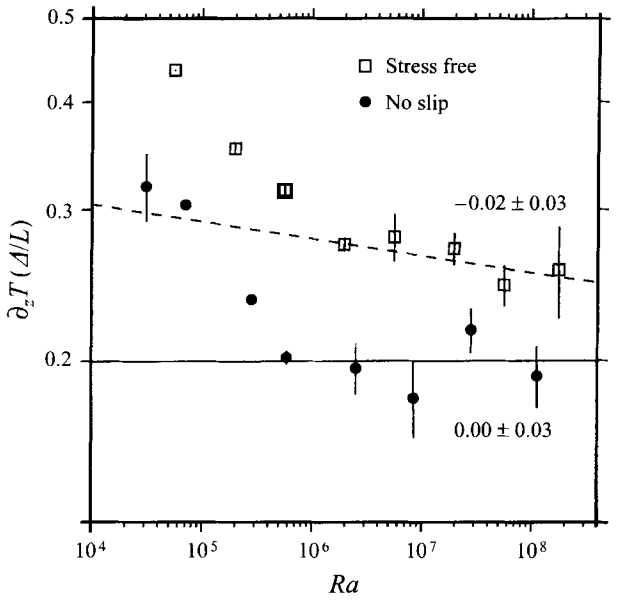

FIGURE 11. Mean negative thermal gradient at mid-layer versus Ra for both stress-free and no-slip boundary conditions; $[Ra/(\sigma Ta)]^{1/2} = 0.75$. Within experimental uncertainty, both series exhibit gradients which asymptote to a finite value at high Ra, though a slight trend in the stress-free solutions may be apparent.

be vortical (see §3.2 above). The second step involves the dynamics of interacting vortices. For the simplest example of line vortices (two-dimensional flow), oppositely signed vortices propagate together on a curved path, the curvature depending on the relative strengths of the two vortex lines, while like-signed filaments circulate about each other (Thompson 1867; Lamb 1932). Because rotating convection between plane boundaries is made up of predominantly cyclonic plumes, the predominant vortex dynamics is the co-rotation of like-signed vortex filaments. Of course three- and more-vortex interactions also occur; see figure 12.

McWilliams (1984) discusses the tendency of decaying two-dimensional and geostrophic turbulence to clump regions of like-signed vorticity. Melander, Zabusky & McWilliams (1988) quantify the conditions required for two symmetric like-signed vortex patches to merge in two dimensions via a Hamiltonian moment model, demonstrating that vortices which are sufficiently close merge. In order to conserve energy, the merger is necessarily accompanied by the shedding of vorticity filaments from the patches. Because all plumes are cyclonic, i.e. have the same sign of vorticity, plumes attract other plumes as they co-rotate (though the merger dynamics of a multi-vortex system with vortices of different sizes and intensities is inherently richer than that of two symmetric isolated vortex patches, as is studied in Melander *et al.*). This is demonstrated graphically in figure 12 which shows the merger of three regions of high vorticity near the bottom boundary. Similar merger events have been reported for laboratory experiments by Zhong *et al.* (1993).

The stirring action of both the co-rotation of plumes and plume mergers is to mix the fluid in horizontal planes. It is this *lateral* mixing which is responsible for the mean thermal gradient presented in figure 10: if a warm fluid element mixes with the surrounding fluid at a given level, it loses its density contrast (and hence its buoyancy) with respect to that level. In turn, the surrounding fluid becomes warmer than if the

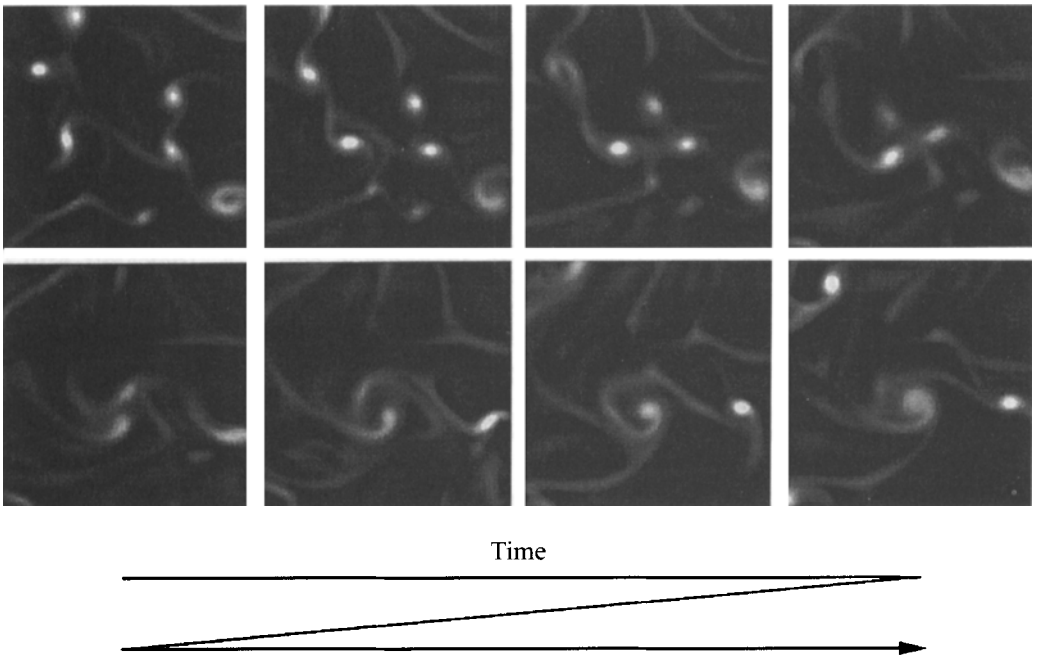

FIGURE 12. Merger of three vortex filaments over a no-slip boundary. $Ra = 8.4 \times 10^6$. Temperature on a plane just above the hot boundary layer is shown with lighter shades depicting hotter fluid. Since plumes intensify cyclonic vorticity, the light spots also indicate vorticity filaments.

lateral mixing had not occurred. Fewer buoyant elements survive at greater distances from the boundaries and the result is a mean temperature stratification with warmer (cooler) fluid near the bottom (top) boundary.

The fact that the mean gradient for the stress-free solutions is somewhat larger than that for the no-slip solutions indicates that Ro is effectively smaller (either because t_W is larger or t_R is smaller) for the stress-free solutions. Here we connect larger mean gradients with stronger rotation since non-rotating convection does not possess a mean thermal gradient. Physically, we might expect t_W to be larger for the stress-free solutions since Ekman pumping enhances vertical transport (and therefore reduces t_W) for the no-slip solutions. Also, t_R for individual plumes is plausibly smaller for the stress-free solutions given that during their formation (and associated spin-up) they need not overcome viscous stresses in the boundary layers as do plumes in the no-slip solutions. Both effects are present at convective onset and are evident in the greater buoyancy forcing required to destabilize the stress-free fluid layer at high Ta; see figure 1.

Since the effectiveness of the lateral mixing induced by the vortex interactions is strongly dependent on the ratio of the timescale associated with vortex motions to that associated with vertical convective transport through the layer, the temperature gradient in the interior is likely to be strongly dependent on the value of the convective Rossby number. This dependence is examined in greater detail in Julien *et al.* (1996*b*).

4. Conclusion

Rapidly rotating turbulent Boussinesq convection, like non-rotating convection, is dominated by coherent plumes when Ra is sufficiently high. If the rotation timescale of the fluid layer is comparable to the characteristic convection timescale, i.e. $Ro \lesssim 1$, the dynamics of individual plumes are dominated by strong vortex–vortex interactions with neighbouring plumes, all of which are cyclonic. The impact of these vortical interactions include vigorous lateral mixing throughout the fluid layer and the establishment of a mean temperature gradient which depends on Ro, σ, and the surface boundary conditions. Additional numerical and experimental work is required to deduce the form of the dependence on each of these parameters.

Despite the dramatic differences between rotating and non-rotating convecting flows (vortical interactions, mean thermal gradient, Ekman pumping, etc.), the scaling on Ra exhibited by Nu, W_c, and Δ_c is identical to that found for non-rotating convection. In particular, we find $Nu \propto Ra^{2/7}$, i.e. the heat-transport law for hard-turbulent convection, despite the presence of strong rotation in our solutions. This suggests that hard turbulence is more ubiquitous in turbulent thermal convection than previously appreciated.

Our long-term goal of this and future work is to improve our understanding of rotation and convection in geophysical and astrophysical flows. At present, attempts to model such flows incorporate large-eddy simulation (LES) or subgrid-scale (SGS) models which do not explicitly resolve small-scale phenomena such as turbulent convective mixing. Instead, parameterizations are utilized to model the subgrid-scale behaviour; often such parameterizations are based on properties of non-rotating turbulence. Here we demonstrate (i) that inhomogeneous mixing is an inherent part of rotating convection, and (ii) that the global statistics and transport properties of hard turbulence are ubiquitous to turbulent convection; these results should be incorporated into parameterization schemes for flows influenced by rotation and/or convection.

We gladly acknowledge useful discussions with Nic Brummell, Peter Fox, John Hart, Scott Kittelman, Dan Ohlsen, Peter Sullivan, and Juri Toomre. K.J. and S.L. are supported by the High Performance Computation and Communication grant ECS9217394. Computations were carried out at the Pittsburgh Supercomputing Center (PSC) under grant MCA935010P. NCAR is sponsored by the National Science Foundation.

Appendix A. Numerical algorithm

Solutions to the Navier–Stokes equations (2.1)–(2.3) are computed between either no-slip or stress-free boundaries using a pseudospectral Fourier–Chebyshev-'tau' method (with 'tau'-corrections). The timestepping algorithm is the mixed implicit/explicit, third-order Runge–Kutta scheme of Spalart, Moser & Rogers (1991), which takes the form

$$\frac{\gamma}{\delta t}\boldsymbol{v}^{n+1} + \boldsymbol{f}^{n} = \sigma\nabla^2\boldsymbol{v}^{n+1} - \nabla P^{n+1} + \sigma\frac{Ra}{16}T^{n+1}\hat{\boldsymbol{z}}\,, \tag{A 1}$$

$$\frac{\gamma}{\delta t}T^{n+1} + s^{n} = \nabla^2 T^{n+1}\,, \tag{A 2}$$

$$\nabla\cdot\boldsymbol{v}^{n+1} = 0\,. \tag{A 3}$$

Here n and $n+1$ refer to sequential time levels for the numerical integration, and δt is the timestep. γ is a constant (different for each Runge–Kutta substep), and the functions $\boldsymbol{f}^n$ and s^n represent all terms at time level n *and earlier*; this includes the explicitly treated nonlinear terms, as well as contributions to the linear terms from previous timesteps. See the appendix of Spalart *et al.* (1991) for details. The timestep δt is variable, selected in accord with the maximum velocity/grid-spacing ratio $U = \max|v/\delta r|$ and the Courant–Friedrichs–Lewy (CFL) condition: $\delta t = CFL/U$. We typically use values of CFL between 0.65 and 0.70 (for the full, 3-level Runge–Kutta timestep). v is one component of the flow velocity and δr the grid spacing parallel to that velocity component, both evaluated at the same spatial location.

Spatial discretization is accomplished with the decomposition of the flow fields into Fourier–Chebyshev coefficients; e.g.

$$\boldsymbol{v} = \sum_{\boldsymbol{k}} \boldsymbol{v}_{\boldsymbol{k}}(z)\, \mathrm{e}^{-\mathrm{i}\boldsymbol{k}\cdot\boldsymbol{x}} = \sum_{\boldsymbol{k},j} \boldsymbol{v}_{\boldsymbol{k}j}\, \mathrm{e}^{-\mathrm{i}\boldsymbol{k}\cdot\boldsymbol{x}}\, T_j(z)\,, \tag{A 4}$$

where $\boldsymbol{k} = (k_x, k_y, 0)$ is the horizontal wave-vector, $\boldsymbol{x} = (x, y, z)$ is the position vector, and $T_j(z)$ is the jth-order Chebyshev polynomial. Rearranging (A 1)–(A 3), then substituting (A 4), we obtain the 'continuous in z' form of the discrete evolution equations for the Fourier coefficients:

$$(\mathrm{D}^2 - \eta)\, T_{\boldsymbol{k}}^{n+1} = s_{\boldsymbol{k}}^n\,, \tag{A 5}$$

$$(\mathrm{D}^2 - \xi)\, U_{\boldsymbol{k}}^{n+1} = -\mathrm{i}k_x \frac{P_{\boldsymbol{k}}^{n+1}}{\sigma} + \frac{f_{1\boldsymbol{k}}^n}{\sigma}\,, \tag{A 6}$$

$$(\mathrm{D}^2 - \xi)\, V_{\boldsymbol{k}}^{n+1} = -\mathrm{i}k_y \frac{P_{\boldsymbol{k}}^{n+1}}{\sigma} + \frac{f_{2\boldsymbol{k}}^n}{\sigma}\,, \tag{A 7}$$

$$(\mathrm{D}^2 - \xi)\, W_{\boldsymbol{k}}^{n+1} = \mathrm{D}\frac{P_{\boldsymbol{k}}^{n+1}}{\sigma} + \frac{f_{3\boldsymbol{k}}^n}{\sigma} - \frac{Ra}{16} T_{\boldsymbol{k}}^{n+1}\,, \tag{A 8}$$

$$(\mathrm{D}^2 - k^2)\, \frac{P_{\boldsymbol{k}}^{n+1}}{\sigma} = -\left(\frac{\nabla\cdot\boldsymbol{f}^n}{\sigma}\right)_{\boldsymbol{k}} + \frac{Ra}{16}\mathrm{D}T_{\boldsymbol{k}}^{n+1}\,. \tag{A 9}$$

Here, $k^2 = \boldsymbol{k}\cdot\boldsymbol{k}$, $\eta = k^2 + \gamma/\delta t$, and $\xi = k^2 + \gamma/(\sigma\delta t)$. D represents differentiation in the z-direction. To solve this system, we begin by solving the linear Helmholtz equation for $T_{\boldsymbol{k}}^{n+1}$ (A 5), subject to fixed-temperature boundary conditions (2.6). Then, with the temperature at the future time known, we evaluate the right-hand sides of (A 8) and (A 9) pseudospectrally (by computing the nonlinear terms in physical-space, followed by a transformation (FFT) back to Fourier-space). The result is a system of the form

$$(\mathrm{D}^2 - \xi)\, W_{\boldsymbol{k}}^{n+1} = \frac{\mathrm{D}P_{\boldsymbol{k}}^{n+1}}{\sigma} + r_{1\boldsymbol{k}}\,, \tag{A 10}$$

$$(\mathrm{D}^2 - k^2)\, \frac{P_{\boldsymbol{k}}^{n+1}}{\sigma} = r_{2\boldsymbol{k}}\,, \tag{A 11}$$

$$W_{\boldsymbol{k}}^{n+1}(\pm 1) = 0\,, \tag{A 12}$$

$$\mathrm{D}W_{\boldsymbol{k}}^{n+1}(\pm 1) = 0 \quad \text{or} \quad \mathrm{D}^2 W_{\boldsymbol{k}}^{n+1}(\pm 1) = 0\,. \tag{A 13}$$

The solution to this system can be obtained using the influence-matrix technique (Kleiser & Schumann 1980; Werne 1995), involving the linear combination of particular and homogeneous solutions that satisfies the boundary conditions of W (A 12)–(A 13) simultaneously. The result is a 2×2 influence-matrix problem for each wavevector $\boldsymbol{k}$. Once (A 10)–(A 13) is solved, the right-hand sides of (A 6)–(A 7) can

be evaluated and those equations solved for U_k^{n+1} and V_k^{n+1}. The solution at later timesteps is obtained by repeating the procedure.

When solving (A 10)–(A 13), we represent the z-dependence by expanding the Fourier coefficients in Chebyshev polynomials; see (A 4). Substitution of (A 4) into (A 10)–(A 13) leads to a linear system of algebraic relations coupling the Chebyshev modes. To incorporate the boundary conditions, we employ the 'tau' approximation, in which equations for the two highest Chebyshev modes are neglected in lieu of conditions at the two boundaries. It has been noted that care must be taken to correctly handle the truncation errors incurred on neglecting the two highest-mode equations (Kleiser & Schumann 1980; Werne 1995). In particular, truncation errors in (A 10)–(A 11) can propagate to all of the mode equations through differentiation of the pressure field in (A 10). Although Kleiser & Schumann (1980) devise a scheme for avoiding the propagation of these errors, they miss a subtle point in the application of the influence matrix method, leading to relative errors in the divergence field of the order of 1%. The correct approach, which points out this subtle oversight and leads to errors at the level of numerical precision (i.e. machine round-off), has been formulated by Werne (1995).

Appendix B. Linear thermal Ekman layer

Consider a fluid layer of semi-infinite extent, bounded below by either a no-slip or stress-free surface. Let us model a hot thermal boundary layer on this surface with the temperature field

$$T = \begin{cases} 1 - z/\lambda & (z < \lambda) \\ 0 & (z \geqslant \lambda) \end{cases} .$$

This temperature field possesses a constant gradient within the boundary layer and is uniform in the interior region away from the surface. The depth of the boundary layer λ is a function of the horizontal coordinates x and y.

Assuming the motions are slow, i.e. neglecting nonlinear and time-derivative terms, the momentum equation becomes

$$-\sigma \left(\frac{Ta}{16}\right)^{1/2} v \approx \sigma \partial_{zz} u - \partial_x P , \tag{B 1}$$

$$\sigma \left(\frac{Ta}{16}\right)^{1/2} u \approx \sigma \partial_{zz} v - \partial_y P , \tag{B 2}$$

$$\partial_z P \approx \sigma \frac{Ra}{16} T . \tag{B 3}$$

Equations (B 1)–(B 3) express the 'boundary-layer' approximation wherein horizontal derivatives are assumed small compared to vertical ones. Also, note that this equation set is identical to that considered in the classical Ekman-layer problem (Gill 1982), apart from the finite vertical pressure gradient required here to balance the thermal stratification.

Defining the following quantities:

$$X = u + \mathrm{i}v , \qquad q = \tfrac{1}{2}(-Ta)^{1/4} , \qquad \text{and} \qquad \Lambda = \frac{Ra}{32}(\partial_x \lambda + \mathrm{i}\partial_y \lambda) ,$$

and substituting into (B 1)–(B 3), we obtain

$$\partial_{zz}X - q^2X \quad = \quad [\partial_{zz}X - q^2X]_{z=0} \quad + \quad \begin{cases} \Lambda(z/\lambda)^2 & (z < \lambda) \\ \Lambda & (z \geqslant \lambda) \end{cases} .$$

Solving these equations subject to the following conditions:

$$X(z=0) = \begin{cases} 0 & \text{no slip} \\ X_0 & \text{stress free} \end{cases}, \quad \partial_z X(z=0) = \begin{cases} \partial_z X_0 & \text{no slip} \\ 0 & \text{stress free} \end{cases},$$

$$X \quad \text{and} \quad \partial_z X \quad \text{finite and continuous,}$$

we obtain

$$X = X_E + X_{th} ,$$

where

$$X_E = \begin{cases} q^{-1}\partial_z X_0 \ (1 - \mathrm{e}^{-qz}) & \text{no slip} \\ X_0 & \text{stress free} \end{cases} \tag{B 4}$$

and

$$X_{th} = \begin{cases} (\Lambda/q^4\lambda^2)(1+q\lambda)\mathrm{e}^{-q\lambda}\,(\mathrm{e}^{qz} + \mathrm{e}^{-qz} - 2) - (\Lambda/q^2)\,(z/\lambda)^2 & (z < \lambda) \\ (\Lambda/q^4\lambda^2)\left\{\left(2 - q^2\lambda^2\right) - 2(1+q\lambda)\mathrm{e}^{-q\lambda}\right. & \\ \qquad \left. + \left[(1+q\lambda)\mathrm{e}^{-q\lambda} - (1-q\lambda)\mathrm{e}^{q\lambda}\right]\mathrm{e}^{-qz}\right\} & (z \geqslant \lambda) \end{cases} \tag{B 5}$$

Note that X_E for the no-slip problem is the classical Ekman solution. If $\Lambda = 0$, i.e. the temperature field is homogeneous (or at least horizontally uniform), then the solution is simply $X = X_E$. On the other hand, if $\Lambda \neq 0$, then the classic Ekman solution is superposed with a thermal solution, which is identical for both the stress-free and no-slip problems.

To illustrate the thermal solution, figure 13 shows a surface plot of the assumed thermal boundary layer shape $\lambda(x, y)$, superposed with contours of the horizontal divergence associated with (B 5) on a single plane beneath the 'plume' (in this case, a Gaussian bump). The qualitative features in the horizontal divergence are independent of height below the tip of the plume. The centre of the plume possesses a positive horizontal divergence, indicating Ekman suction *towards* the boundary on the plume axis. Hence, the core region of the plume opposes the tendency of the classical Ekman pumping effect near a no-slip boundary (see the main body of this paper for a description of the classic Ekman pumping effect). In contrast, figure 13 also illustrates a ring of convergent flow at the edge of the plume which does indeed contribute to Ekman pumping away from the boundary. With the structure of the horizontal divergence, one can guess the behaviour of a full nonlinear solution. The nonlinear advection of temperature (towards the boundary along the plume-axis and away from the boundary within the ring) would tend to reshape a plume into a ring-shaped ridge rather than an individual bump. Of course, this would be counter-balanced by buoyancy in a full nonlinear solution; nevertheless, plumes in a rotating environment should be broader than their non-rotating counterparts for this reason. Figure 5 illustrates rotating plumes for solutions with $Ra = 1.8 \times 10^8$ ($Ra = 1.1 \times 10^8$) over stress-free (no-slip) boundaries. The horizontal divergence and the vertical vorticity are also presented. It is noteworthy that the numerical solutions demonstrate strongly cyclonic rings with weaker vorticity in the cores; in contrast, for the linear analysis the core region of a plume is *anti*cyclonic, due to the assumed Gaussian (i.e. non-ring-like)

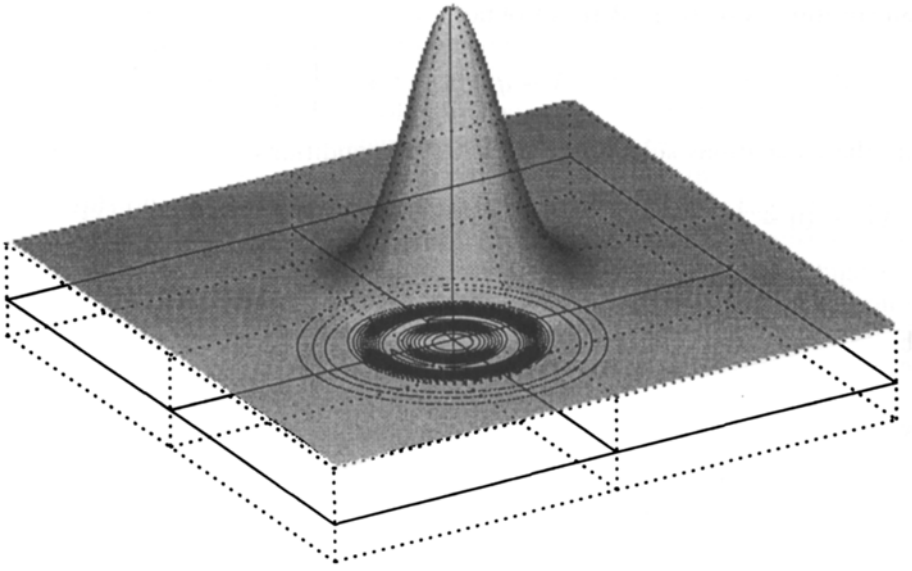

FIGURE 13. Gaussian bump on a thermal boundary layer with associated horizontal divergence. The shaded surface plot depicts the edge of a thermal boundary layer possessing a Gaussian bump. The lower bounding surface is depicted by a dotted plane. Between the bounding surface and the edge of the thermal boundary layer lies a plane on which the horizontal divergence of the flow is shown. The Solid, inner contours depict divergent flow, while the dotted, outer contours display convergent flow. The qualitative features in the horizontal divergence are independent of height below the tip of the "plume." The convergent flow in the plane is associated with flow up away from the bottom bounding surface, while the divergent flow in the core of a plume is associated with downward fluid motion directed towards the bottom boundary.

shape of the thermal anomaly, which concentrates too great a pressure in the plume interior; see (B 3).

Though the qualitative structure of rotating plumes is revealed by this simple linear analysis, it should be clear what drawbacks remain. The major drawback in this analysis is the *a priori* prescription of the temperature field, rather than its self-consistent calculation within a general theory. This of course would be difficult, requiring inclusion of the nonlinear terms since boundary layers are maintained only through nonlinear processes. As a result, the solution presented in this Appendix should not be considered a general solution to the linear equations (B 1)–(B 3), but rather an illustration of the qualitative behaviour specific to rotating thermal boundary layers. Indeed, (B 1)–(B 3) possess no general solution since they represent only three equations of four unknowns.

REFERENCES

ADRIAN, R. J., FERREIRA, R. T. D. S. & BOBERG, T. 1986 Turbulent thermal convection in wide horizontal fluid layers. *Exps. Fluids* **4**, 121–141.

BELMONTE, A., TILGNER, A. & LIBCHABER, A. 1993 Boundary layer length scales in thermal turbulence. *Phys. Rev. Lett.* **70**, 4067–4070.

BOUBNOV, B. M. & GOLITSYN, G. S. 1986 Experimental study of convective structures in rotating fluids. *J. Fluid Mech.* **167**, 503–531.

BOUBNOV, B. M. & GOLITSYN, G. S. 1990 Temperature and velocity field regimes of convective motions in a rotating plane fluid layer. *J. Fluid Mech.* **219**, 215–239.

BRUMMELL, N. H., TOOMRE, J. & HURLBERT, N. E. 1996 Turbulent compressible convection with rotation. Part I: Overview, model and flow structure. Submitted to *Astrophys. J.*

BUSSE, F. H. 1978 Nonlinear properties of thermal convection. *Rep. Prog. Phys.* **41**, 1929–1967.

BUSSE, F. H. 1983 A model of mean zonal flows in the major planets. *Geophys. Astrophys. Fluid Dyn.* **23**, 153–174.

BUSSE, F. H. & CLEVER, R. M. 1979 Nonstationary convection in a rotating system. In *Recent Developments in Theoretical and Experimental Fluid Mechanics, Compressible and Incompressible Flows* (ed. U. Muller, K. G. Roesner & B. Schmidt), pp. 376–385. Springer.

CABOT, W., HUBICKYJ, O., POLLACK, J. B., CASSEN, P. & CANUTO, V. M. 1990 Direct numerical simulations of turbulent convection: I. Variable gravity and uniform rotation. *Geophys. Astrophys. Fluid Dyn.* **53**, 1–42.

CABOT, W. & POLLACK, J. B. 1992 Direct numerical simulations of turbulent convection: II. variable gravity and differential rotation. *Geophys. Astrophys. Fluid Dyn.* **64**, 97–133.

CANUTO, C., HUSSAINI, M. Y., QUATERONI, A. & ZANG, T. A. 1987 *Spectral Methods in Fluid Dynamics.* Springer.

CARRIER, G. F. 1971 Swirling flow boundary layers. *J. Fluid Mech.* **49**, 133–144.

CASTAING, B., GUNARATNE, G., HESLOT, F., KADANOFF, L., LIBCHABER, A., THOMAE, S., WU, X.-Z., ZALESKI, S. & ZANETTI, G. 1989 Scaling of hard thermal turbulence in Rayleigh–Bénard convection. *J. Fluid Mech.* **204**, 1–39.

CHANDRASEKHAR, S. 1953 The instability of a layer of fluid heated below and subject to Coriolis forces. *Proc. R. Soc. Lond.* A **217**, 306–327.

CHANDRASEKHAR, S. 1961 *Hydrodynamic and Hydromagnetic Stability.* Oxford University Press.

CHRISTIE, S. L. & DOMARADZKI, J. A. 1993 Numerical evidence for nonuniversality of the soft/hard turbulence classification for thermal convection. *Phys. Fluids* A **5**, 412–421.

CHRISTIE, S. L. & DOMARADZKI, J. A. 1994 Scale dependence of the statistical character of turbulent fluctuations in thermal convection. *Phys. Fluids* **6**, 1848–1855.

CLEVER, R. M. & BUSSE, F. H. 1979 Nonlinear properties of convection rolls in a horizontal layer rotating about a vertical axis. *J. Fluid Mech.* **94**, 609–627.

CLUNE, T. 1993 Pattern selection in convecting systems. PhD thesis, University of California, Berkley (unpublished).

CLUNE, T. & KNOBLOCH, E. 1993 Pattern selection in rotating convection with experimental boundary conditions. *Phys. Rev.* E **47**, 2236–2550.

CORTESE, T. & BALACHANDAR, S. 1993 Vortical nature of thermal plumes in turbulent convection. *Phys. Fluids* A **5**, 3226–3232.

DEARDORFF, J. W. 1970*a* Preliminary results from numerical integrations of the unstable planetary boundary layer. *J. Atmos. Sci.* **27**, 1209–1211.

DEARDORFF, J. W. 1970*b* Convective velocity and temperature scales for the unstable planetary boundary layer and for Rayleigh convection. *J. Atmos. Sci.* **27**, 1211–1213.

DELUCA, E. E., WERNE, J., ROSNER, R. & CATTANEO, R. 1990 Numerical simulations of soft and hard turbulence: Preliminary results for 2-D convection. *Phys. Rev. Lett.* **64**, 2370–2373.

EKMAN, V. W. 1905 On the influence of the earth's rotation on ocean-currents. *Arkiv. Matem. Astr. Fysik, Stockholm* **2–11**, 1–52.

FERNANDO, H. J. S., BOYER, D. L. & CHEN, R-R. 1989 Turbulent thermal convection in rotating and stratified fluids. *Dyn. Atmos. Oceans* **13**, 95–121.

FERNANDO, H. J. S., CHEN, R.-R. & BOYER, D. L. 1991 Effects of rotation on convective turbulence. *J. Fluid Mech.* **228**, 513–547.

GILL, A. E. 1982 *Atmosphere-Ocean Dynamics.* Academic.

GILMAN, P. A. 1977 Nonlinear dynamics of Boussinesq convection in a deep rotating spherical shell. *Geophys. Astrophys. Fluid Dyn.* **8**, 93–135.

GOLDSTEIN, H. F., KNOBLOCH, E., MERCADER, I. & NET, M. 1994 Convection in a rotating cylinder. Part 2. Linear theory for low Prandtl numbers. *J. Fluid Mech.* **262**, 293–324.

HATHAWAY, D. H., TOOMRE, J. & GILMAN, P. A. 1980 Convective instability when the temperature gradient and rotation vector are oblique to gravity. II. Real fluids with effects of diffusion. *Geophys. Astrophys. Fluid Dyn.* **15**, 7–37.

HELFRICH, K. R. 1994 Thermals with background rotation and stratification. *J. Fluid Mech.* **259**, 265–280.

HESLOT, F., CASTAING, B. & LIBCHABER, A. 1987 Transitions to turbulence in helium gas. *Phys. Rev.* A **36**, 5870–5873.

HIDE, R. 1964 The viscous boundary layer at the free surface of a rotating baroclinic fluid. *Tellus* **XVI**, 523–529.

HOWARD, L. N. 1966 Convection at high Rayleigh number. In *Proc. 11th Intl Congr. of Appl. Mech. Munich (Germany)* (ed. H. Gortler), pp. 1109–1115. Springer.

HOWELLS, P. A. C., ROTUNNO, R. & SMITH, R. K. 1988 A comparative study of atmospheric and laboratory-analogue numerical tornado-vortex models *Q. J. R. Met. Soc.* **114**, 801–822.

INGERSOLL, A. P. 1990 Atmospheric dynamics of the outer planets. *Science* **248**, 308–315.

JONES, H. & MARSHALL, J. M. 1993 Convection in a neutral ocean; a study of open-ocean deep convection. *J. Phys. Oceanogr.* **23**, 1009–1039.

JULIEN, K., LEGG, S., MCWILLIAMS, J. & WERNE, J. 1996*a* Hard turbulence in rotating Rayleigh-Bénard convection. *Phys. Rev.* E **53**, 5557R–5560R.

JULIEN, K., LEGG, S., MCWILLIAMS, J. & WERNE, J. 1996*b* A statistical analysis on the influence of rotation in Rayleigh-Bénard convection. In preparation.

KERR, R. 1996 Rayleigh number scaling in numerical convection. *J. Fluid Mech.* **310**, 139–179.

KLEISER, L. & SCHUMANN, U. 1980 Treatment of incompressibility and boundary conditions in 3-D numerical spectral simulations of plane channel flows. In *Proc. 3rd GAMM Conf. Numerical Methods in Fluid Mechanics* (ed. E. H. Hirschel), p. 165. Vieweg, Braunschweig.

KLINGER, B. A. & MARSHALL, J. 1995 Regimes and scaling laws for rotating deep convection in the ocean. *Dyn. Atmos. Oceans* **21**, 227–256.

KÜPPERS, G. 1970 The steady finite amplitude convection in a rotating fluid layer. *Phys. Lett.* A **32**, 7–8.

KÜPPERS, G. & LORTZ, D. 1969 Transition from laminar convection to thermal turbulence in a rotating fluid layer. *J. Fluid Mech.* **35**, 609–620.

LAMB, H. 1932 *Hydrodynamics*. Dover.

LI, N. & ECKE, R. E. 1993 Küppers-Lortz transition at high dimensionless rotation rates in rotating Rayleigh-Bénard convection. *Phys. Rev.* E **47**, R2991–R2994.

MALKUS, W. V. R. 1963 Outline of a theory of turbulent convection. In *Theory and Fundamental Research in Heat Transfer* (ed. J. A. Clark). Pergamon.

MAXWORTHY, T. & NARIMOUSA, S. 1994 Unsteady deep convection in a homogeneous rotating fluid. *J. Phys. Oceanogr.* **24**, 865–887.

MCWILLIAMS, J. C. 1971 The boundary layer dynamics of symmetric vortices. PhD thesis, Harvard University (unpublished).

MCWILLIAMS, J. C. 1984 The emergence of isolated coherent vortices in turbulent flow. *J. Fluid Mech.* **146**, 21–43.

MELANDER, M. V., ZABUSKY, N. J. & MCWILLIAMS, J. C. 1988 Symmetric vortex merger in two dimensions: causes and conditions. *J. Fluid Mech.* **195**, 303–340.

NAGAKAWA, Y. & FRENZEN, P. 1955 A theoretical and experimental study of cellular convection in rotating fluids. *Tellus* **7**, 1–21.

OHLSEN, D. R., HART, J. E. & KITTELMAN, S. 1995 Laboratory experiments on rotating turbulent convection. *American Meteorological Society Tenth Conf. on Atmospheric and Oceanic Waves and Stability*, Preprints, pp. 255–256.

OOYAMA, K. 1966 On the stability of the baroclinic circular vortex: a sufficient criterion for instability. *J. Atmos. Sci.* **23**, 43–53.

PRANDTL, L. 1932 Meteorologische Anwendungen der Strömungslehre. *Beitr. Physik Atmos.* **19**, 188–202.

PRIESTLEY, C. H. B. 1959 *Turbulent Transfer in the Lower Atmosphere*. The University of Chicago Press.

RAASCH, S. & ETLING, D. 1991 Numerical simulation of rotating turbulent thermal convection. *Beitr. Phys. Atmosph.* **64**, 185–199.

RILEY, J. J., METCALFE, R. W. & ORSZAG, S. A. 1986 Direct numerical simulations of chemically reacting turbulent mixing layers. *Phys. Fluids* **29**, 406–422.

ROSSBY, H. T. 1969 A study of Bénard convection with and without rotation. *J. Fluid Mech.* **36**, 309–335.

SANO, M., WU, X.-Z. & LIBCHABER, A. 1989 Turbulence in helium-gas free-convection. *Phys. Rev.* A **40**, 6421–6430.

SCHOTT, F., VISBECK, M. & FISCHER, J. 1993 Observations of vertical currents and convection in the central Greenland Sea during the winter of 1988-1989. *J. Geophys. Res.* **98**, 14401–14421.

SHE, Z.-S. 1989 On the scaling laws of thermal turbulent convection. *Phys. Fluids* A **1**, 911–913.

SHRAIMAN, B. & SIGGIA, E. 1990 Heat transport in high-Rayleigh-number convection. *Phys. Rev.* A **42**, 3650–3653.

SOMERVILLE, R. C. F. & LIPPS, F. B. 1973 A numerical study in three space dimensions of Bénard convection in a rotating fluid. *J. Atmos. Sci.* **30**, 590–596.

SPALART, P. R., MOSER, R. D. & ROGERS, M. M. 1991 Spectral methods for the Navier-Stokes equations with one infinite and two periodic directions. *J. Comput. Phys.* **96**, 297–324.

SPIEGEL, E. A. 1971 Convection in stars I. Basic Boussinesq convection. *Ann. Rev. Astron. Astrophys.* **9**, 323–352.

SPIEGEL, E. A. 1972 Convection in stars II. Special effects. *Ann. Rev. Astron. Astrophys.* **10**, 261–304.

STOMMEL, H. 1972 Deep winter-time convection in the western Mediterranean sea. In *Studies in Physical Oceanography: a tribute to Georg Wust on his 80th birthday* (ed. A. L. Gordon), pp. 207–218. Gordon and Breach.

SWIFT, J. 1984 Convection in a rotating fluid layer. *Contemp. Maths* **28**, 435–448.

TAYLOR, G. I. 1923 Experiments on the motion of solid bodies in rotating fluids. *Proc. R. Soc. Lond.* A **104**, 213–218.

THOMPSON, W. 1867 On vortex atoms. *Phil. Mag.* **34**, 20. [Papers iv.1]

TILGNER, A., BELMONTE, A. & LIBCHABER, A. 1993 Temperature and velocity profiles of turbulent convection in water. *Phys. Rev.* E **47**, R2253–R2256.

TONG, P. & SHEN, Y. 1992 Relative velocity fluctuations in turbulent Rayleigh-Bénard convection. *Phys. Rev. Lett.* **69**, 2066–2069.

VERONIS, G. 1968 Large amplitude Bénard convection in a rotating fluid. *J. Fluid Mech.* **31**, 113–139.

WERNE, J. 1993 The structure of hard turbulent convection in two dimensions: numerical evidence. *Phys. Rev.* E **48**, 1020–1035.

WERNE, J. 1995 Incompressibility and no-slip boundaries in the Chebyshev-tau approximation: correction to Kleiser and Schumann's influence-matrix solution. *J. Comput. Phys.* **120**, 260–265.

WERNE, J., DELUCA, E. E., ROSNER, R. & CATTANEO, F. 1991 Development of hard turbulent convection in 2-D numerical simulations. *Phys. Rev. Lett.* **67**, 3579–3581.

WILSON, T. & ROTUNNO, R. 1986 Numerical simulation of a laminar end-wall vortex and boundary layer. *Phys. Fluids* **29**, 3993–4005.

WU, X.-Z., CASTAING, B., HESLOT, F. & LIBCHABER, A. 1988 Scaling properties of soft thermal turbulence in Rayleigh-Bénard convection. In *Universalities in Condensed Matter* (ed. R. Jullien, L. Peliti, R. Rammal & N. Boccara), pp. 208–212. Springer.

WU, X.-Z., KADANOFF, L. P. LIBCHABER, A. & SANO, M. 1990 Frequency power spectrum of temperature-fluctuations in free-convection. *Phys. Rev. Lett.* **64**, 2140–2143.

WU, X.-Z. & LIBCHABER, A. 1992 Scaling relations in thermal turbulence – the aspect-ratio dependence. *Phys. Rev.* A **45**, 842–845.

YAKHOT, V. 1992 4/5 Kolmogorov law for statistically stationary turbulence: application to high-Rayleigh-number Bénard convection. *Phys. Rev. Lett.* **69**, 769–771.

ZHONG, F., ECKE, R. & STEINBERG, V. 1993 Rotating-Bénard convection: asymmetric modes and vortex states. *J. Fluid Mech.* **249**, 135–159.

ZOCCHI, G., MOSES, E. & LIBCHABER, A. 1990 Coherent structures in turbulent convection, an experimental-study. *Physica* A **166**, 387–407.